STATIC AND DYNAMIC CALIBRATION OF A MULTI-COMPONENT SIDEWALL FORCE BALANCE FOR A TRANSONIC LUDWIEG TUBE WIND TUNNEL

by

MICHAEL GERARD WERLING JR

Presented to the Faculty of the Graduate School of
The University of Texas at Arlington in Partial Fulfillment
of the Requirements
for the Degree of

MASTER OF SCIENCE IN AEROSPACE ENGINEERING

THE UNIVERSITY OF TEXAS AT ARLINGTON

December 2011

I would like to dedicate the work presented to my family, my friends, and my professors. My family for their support throughout all of my educational career; my friends for their inspiration to keep moving forward through the hard times; and my professors for pushing me to my limits while still expecting my best work.

ACKNOWLEDGMENTS

I would like to thank my many professors throughout my educational career, especially Dr. Lu, Dr. Wilson, and Dr. Maddalena for their support and guidance throughout my graduate career, as well as pushing me to do my best while also understanding the basics. I would also like to thank the ARC family, including Eric Braun, Dibesh Joshi, and Andrew Mizener for putting up with my many questions during my short tenure, as well as Jeiny Gutierrez for her assistance with running the transonic facility and analyzing some of the data. Lastly, I would like to thank my family and closest friends for their support and inspiration throughout my graduate career.

November 30, 2011

ABSTRACT

STATIC AND DYNAMIC CALIBRATION OF A MULTI-COMPONENT SIDEWALL FORCE BALANCE FOR A TRANSONIC LUDWIEG TUBE WIND TUNNEL

MICHAEL GERARD WERLING JR, M.S.

The University of Texas at Arlington, 2011

Supervising Professor: Dr. Frank Lu

Experimentation involving transonic flow requires replicating not only the Mach number but also the Reynolds number. Improper matching of the Reynolds number affects the interaction between the shocks and boundary layer on the surface of an airfoil, moving the position of the shock and altering the downstream flow field. Both Mach and Reynolds numbers have a large influence on the lift and drag characteristics of airfoils, amongst other aerodynamic effects, within the transonic regime of flight.

A strain-based, multi-component, sidewall force balance was purchased in 1989 specifically for the transonic Ludwieg tunnel at the University of Texas–Arlington, but proper calibration has not been applied since 1990. Dynamic loads are experienced by the balance, so to ensure that the force balance measures forces and moments properly, static and dynamic calibrations are necessary to eliminate the interference from the tunnel on the balance and the model. The procedures for static and dynamic calibration of the force balance are the main topics of discussion, including calculations, results, and uncertainty analysis.

After calibration, a parametric study was completed on a NACA 0012 wingtip showing the changes in the coefficients of lift and drag with the angle of attack. A comparison was also made with data from a two-dimensional NACA 0012 wing from NASA.

TABLE OF CONTENTS

LIST OF ILLUSTRATIONS

LIST OF TABLES

NOMENCLATURE

C_L	lift coefficient
C_D	drag coefficient
C_M	moment coefficient
C_N	normal coefficient
C_A	axial/chord coefficient
ρ	density, kg/m^3 [lbm/ft^3]
V	airspeed velocity, m/s [ft/s]
l	characteristic length, m [ft]
F	force, N [lbf]
t	time, s
T	temperature, K [°R]
q	dynamic pressure, kPa [psi]
Re	$=\rho VL/\mu$, Reynolds number
P	static pressure, kPa [psi]
$\mathbf{M}$	balance matrix
μ	viscosity, kg/m·s [lbm/ft·s]
c	chord length, m [in.]
S	planform area, m^2 [in^2]
L	lifting force, N [lbf]
D	drag force, N [lbf]
NF	normal force component, N [lbf]
CF	axial/chord force component, N [lbf]

MX	moment about X-axis, N· m [lbf·in.]
MZ	moment about Z-axis, N· m [lbf·in.]
PM	pitching moment, N· m [lbf·in.]
$R1$	reading from strain bridge 1 corresponding to NF and MX, V
$R2$	reading from strain bridge 2 corresponding to NF and MX, V
$R3$	reading from strain bridge 3 corresponding to CF, V
$R4$	reading from strain bridge 4 corresponding to MZ, V
$R5$	reading from strain bridge 5 corresponding to PM, V
M	freestream Mach number
a	freestream speed of sound, m/s [ft/s]
γ	specific heat ratio
R	specific gas constant, J/mol· K [BTU/mol·°R]
α	angle of attack, deg [°]
S	sensitivity constant, lbf/mV or lbf·in./mV
x	Cartesian coordinate along streamwise length, m [in.]
y	Cartesian coordinate along spanwise width, m [in.]
z	Cartesian coordinate along transverse height, m [in.]

Subscripts

o	total

CHAPTER 1

INTRODUCTION

1.1 Background

Wind tunnels are still necessary for the development of aerospace vehicles despite the substantial use of computational fluid dynamics. While much cutting-edge research has focused on the hypersonic regime, large transonic transports continue to evolve and is a mainstay of the aerospace industry in the US. This evolution places demands on understanding the aerodynamics of advanced designs. The high Reynolds number[1] in the transonic flight regime of large transports requires duplication of both Mach and Reynolds numbers in aerodynamic testing for accurate results due to shock-boundary layer interaction affecting the position of the shock on the wing. Since wind tunnels test at subscales, high Reynolds number can be achieved by raising the pressure to over 1000 kPa. A class of facility that is capable of doing precisely this is the Ludwieg tube wind tunnel.

For transonic testing of large transports, modern industrial practice is to use large cryogenic wind tunnels to approach if not match the fullscale Reynolds number, leaving the Ludwieg tube out of favor. Now, the Reynolds number is given by

$$Re = \frac{\rho V l}{\mu} \tag{1.1}$$

indicating that to achieve a large value, the temperature T can be decreased which raises the density ρ and lowers the viscosity μ. This principle is used in cryogenic tunnels. Alternatively, the pressure can be increased, thereby affecting the density directly. This is the principle used in Ludwieg tube wind tunnels. In passing, some

[1] Greater than 40 million/m.

other ways of increasing the Reynolds number includes the use of a heavy gas or to increase the length scale l by using larger models and test sections.

Matching the Reynolds number between a subscale test model and an actual flight vehicle is crucial in the transonic range due to the extreme sensitivity of the flow to the Reynolds number, see §1.1.2. A mismatch in Reynolds number will yield erroneous aerodynamic data rendering them useless for design purposes. There have been numerous instances where poor prediction of transonic flight characteristics has led to catastrophic failures. Proper duplication is important when trying to reproduce the same flight conditions that are pertinent to conventional military and commercial aircraft within the transonic range. Other than fixed-wing aircraft, transonic aerodynamics is also important in rotorcraft aerodynamics, particularly with regards to the flow past rotor tips [2].

1.1.1 History of the Ludwieg Tube

In 1957, Hubert Ludwieg proposed a wind tunnel concept that subsequently carries his name in an effort to increase the test times of conventional shock tubes [7]. It was subsequently determined in the 1960s that this concept could nearly match the Reynolds numbers of transonic aircraft at that time. This capability should be put in the context of poor matches between predicted performance that was discovered during flight testing that required redesign of many different aircraft such as the C-141, F-111 and the YF-12, the last being the precursor of the SR-71 Blackbird (Fig. 1.1) [8]. The poor predictions could be attributed strongly to wind tunnels of that time which were not capable of replicating the high Reynolds numbers of transonic flight of those cited aircraft [2]. The Ludwieg tube appeared to be the least costly approach for duplicating the proper transonic conditions for developing accurate performance predictions.

Figure 1.1. From left to right, the C-141 Starlifter, the F-111 Aardvark, and the YF-12 Blackbird, precursor to the SR-71 [1].

The Ludwieg tube concept was approved by NASA in 1971 to be a contender for the "National Transonic Facility." Even though the Ludwieg tube was able to produce low turbulent flow, in addition to matching the Mach and Reynolds number of large transonic aircraft, unfortunately, short test times of less than half a second, high dynamic pressures, and high stresses encountered by the models caused some concern and prompted alternatives. The stresses were considerable enough to distort and ruin the scaled models under extreme pressure loading [2].

The idea of using cryogenics to increase the Reynolds number was introduced in 1971, with a pilot version developed, operated, and proven at Langley Research Center in 1973. An in-depth study determined that the two separate facilities, a Ludwieg tube and a cryogenic facility, would be the optimum way to achieve the high Reynolds numbers for development, and the longer test runs and lower dynamic pressures for research, respectively. However, construction costs increased in 1974 when the proposal was sent to Congress, doubling the cost of the Ludwieg tube and bringing cause for its removal from the proposition [8].

1.1.2 Difficulties of Transonic Testing

The unusual flow behavior at transonic speeds creates difficulties both in testing and design since the flow characteristics are mixed, where supersonic and subsonic

fields intermingle. For example, the difficulties in analyzing and learning about the flow around an airfoil at transonic speeds can be seen in Fig. 1.2. Shock waves begin to form over the surfaces, the boundary layer separates, and crucial parameters, such as forces and moments, become difficult to predict. For transonic flow testing, the physical laws may not be directly apparent since the measurements are dependent on the dimensions of both the model and the test section. For this reason, slots, perforations, and porous walls have large roles in producing the necessary conditions for accurate flow within the test section [9].

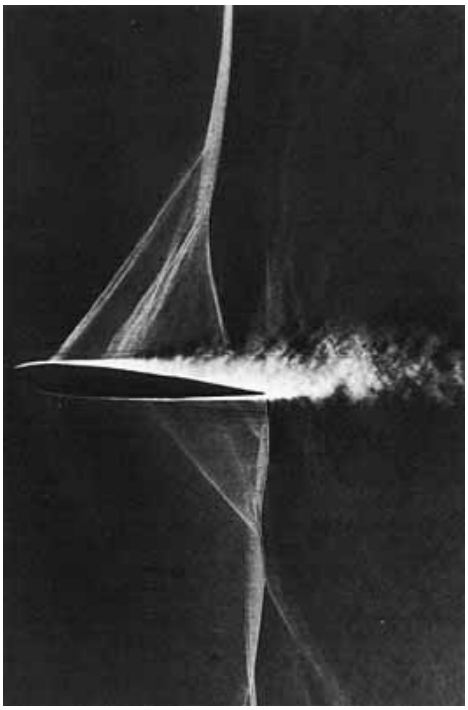

Figure 1.2. Schlieren photograph showing shock waves present on the surfaces of an airfoil and the boundary layer separation [2].

Of particular concern is the high subsonic regime. For example, the flow over rectangular and unswept airfoils creates a large drag force, reduces lift, and creates

strong shock waves. Even though sweeping the wings is not necessary, it does provide a reduction in drag and mitigates the effect of any shocks that form, postponing the severity of the shocks to higher Mach numbers.

The high subsonic flow is sensitive to the surface contour, affecting the location of the shock wave. The interaction between the shock and the boundary layer over the surface has a dominant effect in the aerodynamics. In one instance, the interaction between the shock wave and the boundary layer is less when the boundary layer is turbulent since the incoming boundary layer velocity profile is fuller. Therefore, a lower test Reynolds number which can result in substantial laminar flow over the surface will yield a different flow pattern compared to the higher Reynolds number of full-scale flight. Another possible mismatch occurs even if the flow over the test article is turbulent but at lower Reynolds number than full-scale, also referred to as "Reynolds number effect." For these reasons, the Reynolds number needs to be matched as best as possible when subscale models are used for testing since large differences can change the shock location and the downstream flow field. The Mach number also has influence on the shock position over the airfoil, as seen by the effect of compressibility on the section lift coefficient as a function of Mach number in Fig. 1.3. A significant change in lift between Mach 0.8 and 0.9 is illustrated due to the location of the shock waves and the shock-boundary layer interaction [3].

1.1.3 Objectives of the Research

Based on previous work using the UTA Ludwieg tube by Peeples [10], which involved modifying the pressure lines to obtain more accurate transducer measurements, a constant Mach number throughout the test section was confirmed based on the test section data from Rath [11], Kalkhoran [12], and Starr and Schueler [13]. The constant flow conditions are shown and explained in §2.3.1. The force balance

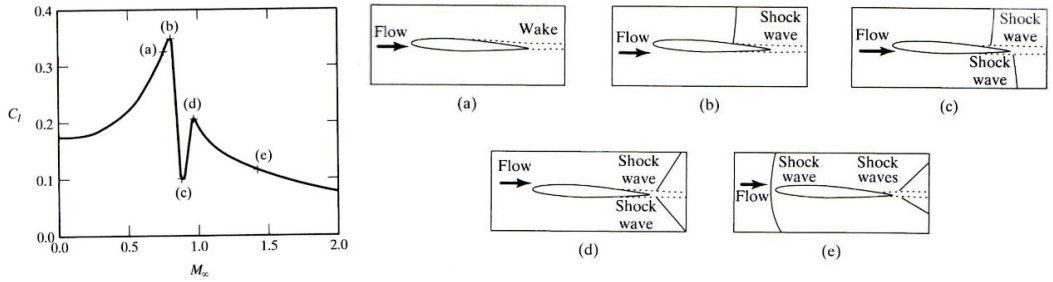

Figure 1.3. Section lift coefficient as a function of Mach number to show the effect of compressibility, with illustrations of the flow field [3].

was originally calibrated by the manufacturer, Modern Machine Tools, Inc., in 1989, recalibrated by Young [14] in 1991, and utilized by Peeples [10] and Elbers [15]. The repeatability of the tunnel conditions was considered high based on the previous work and analysis, but the results from the force balance were not. Based on the work completed by Braun [4], the Ludwieg tube is in operational condition and provides the constant flow conditions necessary for testing.

The force balance is an integral device for this Ludwieg tube, providing aerodynamic load values within the transonic regime. The sensitivity of the balance allows both low and high frequencies to be measured, distorting the output and creating large uncertainties within the data. The dynamic loads experienced by the balance also affect the output, mostly due to the starting process and the sliding sleeve valve in the tunnel, which also causes the tunnel to possibly jolt. The intention is to calibrate the balance for the static loads, eliminate the dynamic interference and, if necessary, compensate for the acceleration created by the tunnel. The test results are compared to other documented data results for lift and drag coefficients, requiring the readings of the normal force, chord force, and pitching moment on the chosen model, a NACA 0012 airfoil.

CHAPTER 2

FACILITY EQUIPMENT AND SETUP

2.1 Introduction

Four wind tunnels, in addition to other facilities, are available at the University of Texas at Arlington's (UTA) Aerodynamics Research Center for research that cover each of the four flow regimes: subsonic, transonic, supersonic, and hypersonic. Each tunnel has its own special qualities, and most of the equipment for each has been customized specifically for that tunnel. The transonic tunnel, in particular, is one of only a handful of Ludwieg tube wind tunnels in the world capable of producing transonic flow.

2.2 Ludwieg Tube Wind Tunnel at UTA

The Ludwieg tube tunnel was acquired as a donation from the Arnold Engineering Development Center (AEDC) in 1978 after it was decommissioned in 1976. The 1/13th scale tunnel has the capability to produce Reynolds numbers up to 400 million/m for chord lengths of approximately 75 mm (3 in.). It was previously used at UTA to study rotorcraft blade/vortex interactions [10, 11, 12] and fighter jet wings [15], since the tunnel is capable of producing Mach numbers between 0.5 and 1.2. While cryogenic wind tunnels have widespread industrial use, this low-cost facility can be used for basic research at transonic speeds [4].

2.2.1 Description

The source of energy for this wind tunnel comes from a charge tube, which is approximately 34 m (111 ft) long with a diameter of about 353 mm (13.9 in.), as seen in the schematic in Fig. 2.1 [16]. This tube can be charged to 5150 kPa (750 psia) to produce a stagnation pressure of 3450 kPa (500 psia). The contraction ratio of the nozzle is 2.27. Additionally, a transition from the circular section of the charge tube to the rectangular test section is afforded in this contraction zone. This constant ratio signifies that a minimum pressure is necessary to obtain the minimum velocity in the test section for a run, which is approximately 690 kPa (100 psia). The principle of the steady flow is mentioned in §2.2.2.

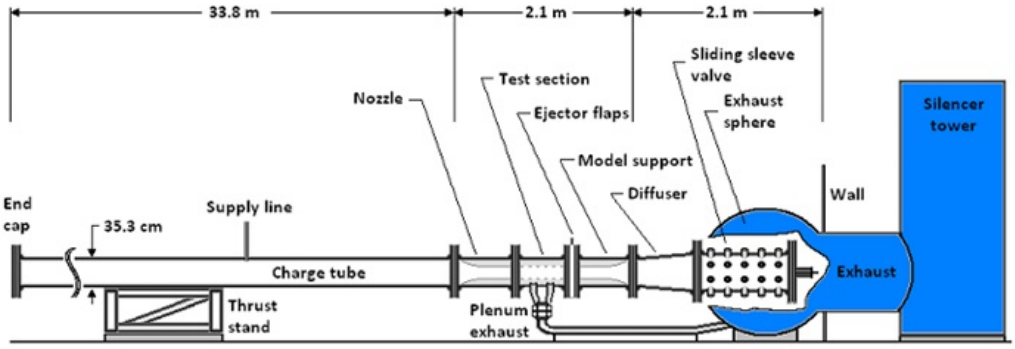

Figure 2.1. A schematic of the UTA Ludwieg tube [4].

The test section (Fig. 2.2) has a rectangular section of 186 mm by 232 mm (7.34 in. × 9.15 in.). It has the option of being surrounded by four porous walls, or two porous top and bottom plates and two solid side walls. A single porous wall consists of two stacked plates with holes inclined at 60 degrees, evenly spaced, to provide uniform porosity. The porosity on each wall can be varied continuously from 3.5% to

10% of the wall area by manually moving one plate relative to the other. A plenum cavity surrounds the test section and has approximately 1.75 times its volume [4].

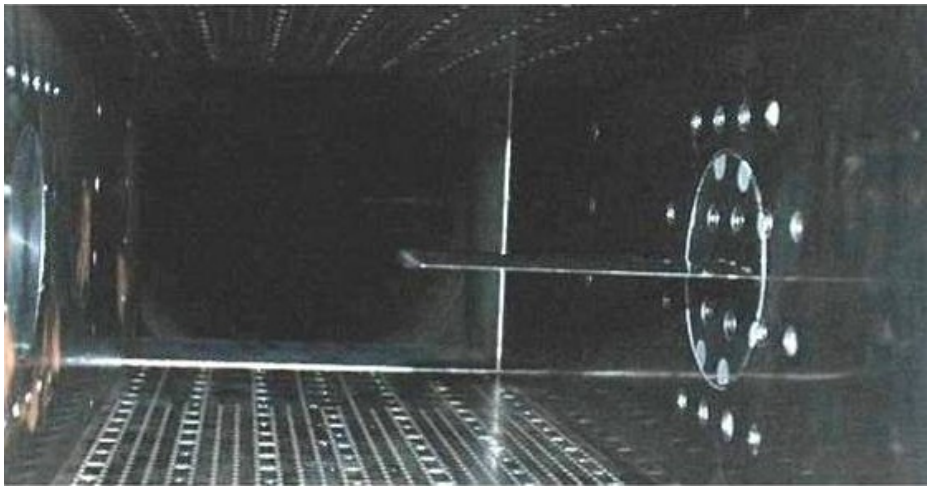

Figure 2.2. Photo of the test section with an airfoil in position for a test run, showing the porous plates on the top and bottom walls.

Referring to Fig. 2.3, the ejector flaps located immediately downstream of the test section allow the flow to become supersonic if they are open. The diffuser section follows, transitioning the cross-section from rectangular back to circular. The plenum exhaust system allows the flow in the plenum cavity to be released to the atmosphere (Fig. 2.4). Eight flex hoses connect the plenum shell to the manifold. Within the manifold is the diaphragm holder, made of two plates that pinch the mylar diaphragms together and allows the pressure to build when filling for a run [16]. When the tunnel is ready to fire, a pneumatic cutter is actuated and punctures the mylar, allowing the pressure to exhaust to the atmosphere at a rate that depends on the position of the variable 6-inch ball valve, controlling the mass flow rate and therefore the Mach number.

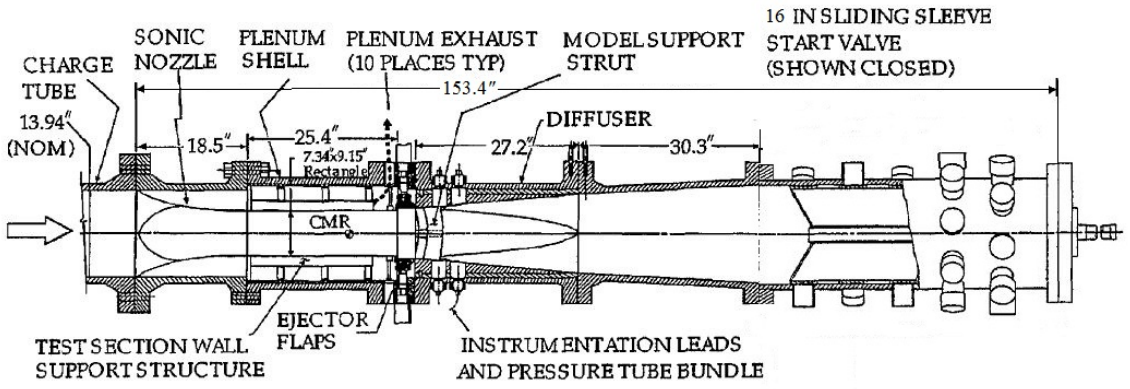

Figure 2.3. A schematic of the main components surrounding the test section [5].

The 16-inch sliding sleeve valve (SSV) is the starting device, operated by a series of pneumatic actuators. The valve contains a total of 45 port caps, but a maximum of 14 ports at any one time can be removed. This is because the choke point of the main flow is in the SSV. If more ports are removed, the choke point moves towards the test section and the Mach number cannot be controlled. When the SSV and the diaphragm are synchronized, expansion waves are able to reach the test section at about the same time, maximizing the test time [16]. There is an optional 12-inch SSV that can be attached, but it is currently not in use.

2.2.2 Principle, Settings & Operation

The general features of a Ludwieg tube are similar to a supersonic blowdown tunnel, with the nozzle and diffuser, but the pressure is built up in the tube, not in a tank. Once the desired charge tube pressure is reached, a valve, downstream of the test section, is actuated and a diaphragm is ruptured, creating an expansion wave that moves from the diffuser through the test section, the nozzle and into the tube [17]. The starting process eventually settles down and the test flow is established

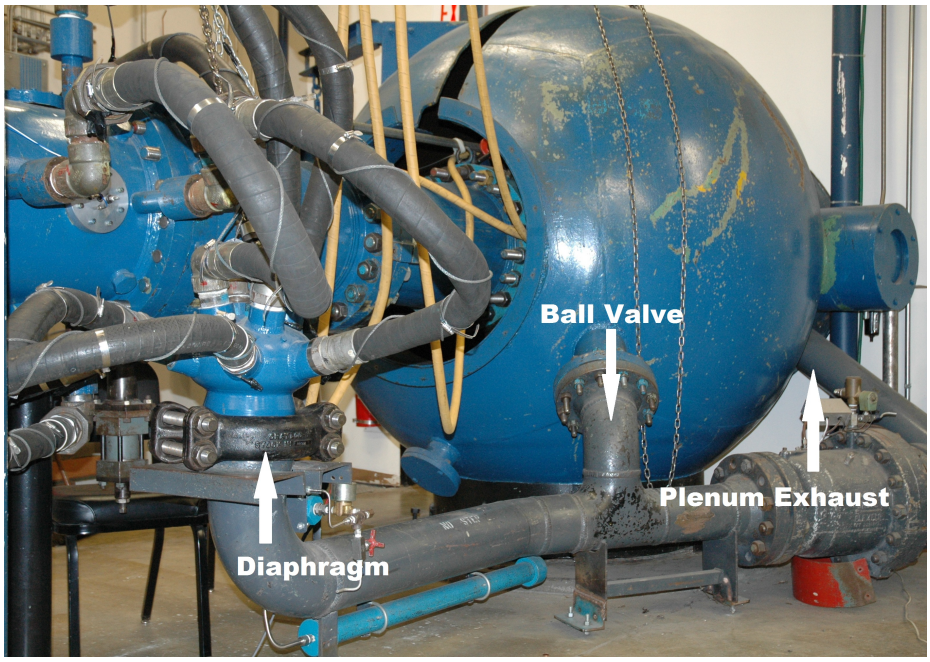

Figure 2.4. Layout of the plenum exhaust system.

with constant properties such as the Mach number, Reynolds number, pressure, and temperature to become constant [7]. The wave automatically reflects off the closed downstream end of the tube, and steady flow is maintained in the test section until the reflected wave returns to the test section. Figure 2.5 [5], shows a schematic of the ideal wave process to establish the test time. The length of the tube directly corresponds to the duration of the test time; the longer the tube, the longer a steady-state run. Once the reflected wave reaches the nozzle again, the test period is completed. It is possible for the reflected wave to travel upstream through the test section a second time, creating a much shorter second test period at approximately the same Mach number but at a Reynolds number about half of the value for the first test period. For this particular Ludwieg tube, the run time ranges between 80 and 120 ms for the first test time, depending on the starting process and length of delay for the SSV and diaphragm [16].

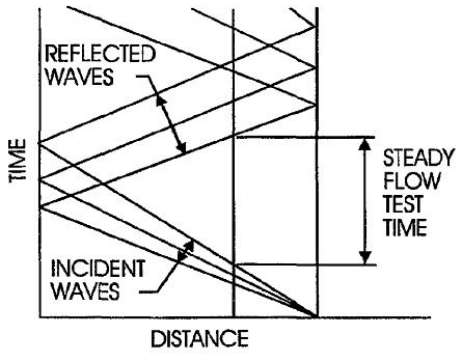

Figure 2.5. A diagram of how the expansion waves operate within the Ludwieg Tube [5].

The number of SSV ports that are opened and the setting of the ball valve, located within the exhaust sphere, control the Mach number and the mass flow rate. The ball valve has 26 positions, where 1 is fully opened and allows more mass flow, therefore increasing the Mach number within the test section. Conversely, position 26 is fully closed, decreasing mass flow and the Mach number in the test section [16]. The ball valve position is currently at 11. The ejector flap opening height increases the test section airspeed, in conjunction with the SSV and the ball valve. When the flaps are opened, and the other settings allow it, the flow in the test section can exceed Mach 1; however, the flaps are currently closed. The wall porosity is also an important setting for the test section Mach number. Decreasing the porosity percentage allows the test section Mach number to increase. Currently the wall porosity is set at 4.5% of the wall area. Table 2.1 lists all of the current Ludwieg tube settings used for this data collection and analysis. For operating instructions of the tunnel, please refer to the manual [16].

The Mach number is controlled by opening ports in the SSV, moving the ball setting, or opening the ejector flaps. The current settings for the wind tunnel allow for a test section Mach number of 0.75. The Reynolds number is directly related to the

Table 2.1. Current Ludwieg tube settings.

Variation	**Setting Used**
Mach Number	0.75
Reynolds Number	5.0 million/inch
SSV Ports Open	11 out of 45
Ball Valve Position	11
Wall Porosity	4.5%
Ejector Flaps	0.0 in.
SSV Delay	0 ms
Plenum Cutter Delay	33 ms

charge pressure, as discussed in §1.1. A graph of how the Reynolds number is related to the charge pressure can be found in Fig. 2.6 [5]. The timing of when the SSV is opened and when the plenum cutter ruptures the diaphragm are the most important aspects of achieving steady run time at the designated Mach number. Currently, the SSV is set with no time delay and the plenum cutter is set at a delay of 33 ms. These settings are due to the fact that the plenum cutter is closer to the test section than the SSV, and the waves need to coalesce in order to create the steady state.

To do a run, a large head pressure is necessary to fill the tube in a reasonable amount of time. For a charge tube pressure of 1200 kPa (175 psia), a storage pressure of more than 6900 kPa (1000 psia) is suggested. The facility uses a 930 kW (1250 hp) 5-stage Clark reciprocating compressor, currently rated at 13.8 MPa (2000 psi). For auxiliary pneumatic controls, a 1200 kPa (175 psig) Kellogg-American compressor is used.

The force balance can only be attached on either side of the test section when the solid walls are in place; porous walls can only be used on the top and bottom of the test section. The angle of attack α of a test article can be set by rotating the bar applied to the base of the balance using a smart angle device; see §2.4 for details.

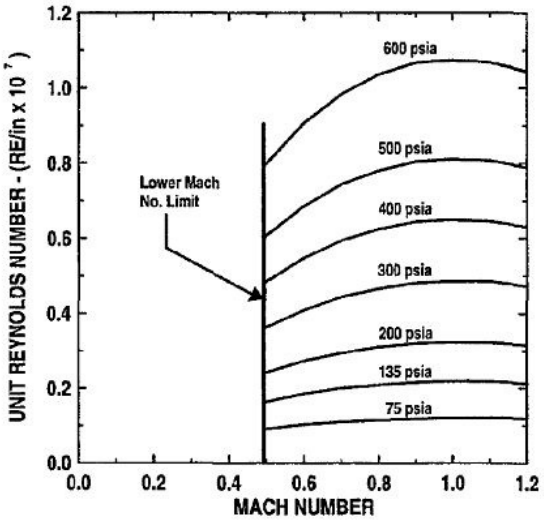

Figure 2.6. Approximate Reynolds number based on the charge pressure and the desired Mach number [5].

The balance is then firmly attached to the tunnel, the angle of attack is confirmed, and the data acquisition system is turned on.

2.3 Data Acquisition

National Instruments (NI) equipment is utilized to read the pressures, temperature, and force balance readings with simultaneous sample-and-hold data acquisition systems (DAQs). The raw data are subsequently reduced to obtain the Mach and Reynolds number and aerodynamic parameters such as forces and moments, as necessary. Currently, pressure readings are taken from a wall tap at the test section, directly across from the model, and the front of the charge tube, which is the entrance to the nozzle. These measure the stagnation and static pressures respectively. The temperature is measured at the front of the charge tube as well. The pressure transducers used to measure the total pressure and the test section pressure are PCB Model 111A24, while for the static pressure an Omega PX313500G5V transducer is used. The thermocouple used is an Omega, Series No. TRP, type K.

The pressure transducers are read by a NI PXI-6133 DAQ card with 14-bit resolution and a maximum sampling rate of 3 MS/s. The SSV is controlled by a PXI-6722 high voltage output card with a 13-bit output resolution. These cards are in a PXI-1036 chassis (Fig. 2.7), which utilizes a PXI-8336 PC control that is connected by fiber-optic cables to the host computer using a PCI-to-PCI bridge that is transparent to both PC hardware and software while still providing high performance [18].

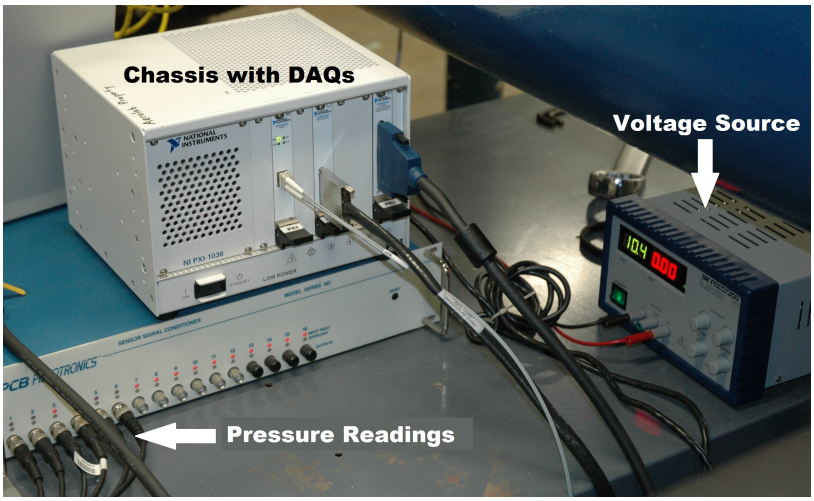

Figure 2.7. Photo of the DAQ setup used.

The force balance and the thermocouple readings are acquired by a PCI-6023E DAQ card with a 12-bit resolution and a maximum sampling rate of 200 kS/s connected directly to the computer. The DAQ card takes the strain gage output from a SCC-2345 Carrier connector block, which houses three SCC-SG04 strain gage modules and one SCC-TC02 thermocouple module (Fig. 2.8). The SCC-SG04 modules are full bridge configurations that have two channels, a signal range from ±100 mV, and a 1.6 kHz low-pass filter. Information on the strain gages within the force balance can be found in §2.4. The SCC-TC02 module also has a signal range of ±100 mV, but has only a 2 Hz low-pass filter [18].

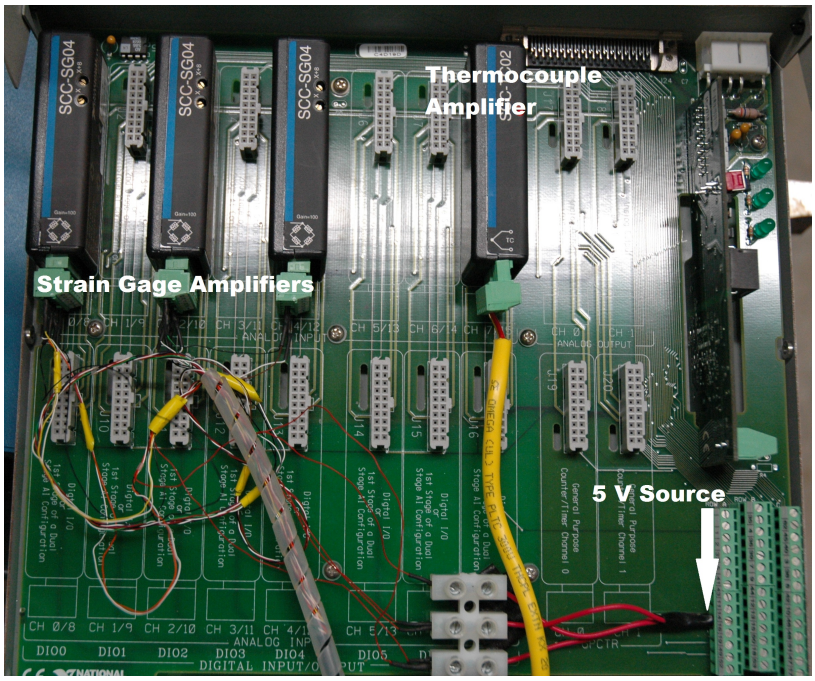

Figure 2.8. Connector block that houses the amplifier modules for gathering the force balance and temperature data.

All control and data acquisition functions are through an in-house NI LabVIEW program, "Transonic." The program allows the sampling rate and sample time to be easily altered for more readings and/or longer read times. Typically only a one second window is needed to gather the data. When the program is run, the SSV is opened and the diaphragm ruptured according the delays specified within the program while simultaneously reading and recording the data. The data are then dumped into an Excel file for analysis.

2.3.1 Data Reduction

The pressure transducers have a factory calibration factor that is accounted for in the analysis. An Excel file is used to convert the voltage signals to pressure units, enabling the calculation of the Mach number, Reynolds number, and the dynamic

pressure of the run. There is a small discrepancy between the transducer signals in the test section, so the pressure values are averaged to obtain the testing conditions. An offset for the pressure and temperature data is accounted for in the reduction. Information on how the force balance data are analyzed can be found in §2.4.

Isentropic conditions and compressible flow theory is used to analyze the data from each run, which utilizes the Mach number as the main parameter. This is possible because air is assumed to behave as a thermally perfect gas, namely,

$$P = \rho RT \tag{2.1}$$

where the specific heats at constant pressure and volume, c_p and c_v, are constant so that the specific heat ratio $\gamma = 1.4$ for air is also a constant. The flow undergoes an isentropic expansion except in viscous regions such as the boundary layer of the tunnel [3]; thus,

$$\frac{P}{\rho^{\gamma}} = \text{const.} \tag{2.2a}$$

$$\frac{T^{(\gamma/\gamma-1)}}{P} = \text{const.} \tag{2.2b}$$

The speed of sound is

$$a = \sqrt{\gamma RT} \tag{2.3}$$

Since the flow is assumed a perfect gas, the isentropic relations yield the test section Mach number in terms of the total and static pressures, namely,

$$M = \sqrt{\frac{2}{\gamma - 1}\left[\left(\frac{P_o}{P}\right)^{(\gamma-1)/\gamma} - 1\right]} \tag{2.4}$$

By similar manipulation, the static temperature in the test section is given by

$$T = T_o\left(1 + \frac{\gamma - 1}{2}M^2\right)^{-1} \tag{2.5}$$

The viscosity can be found using Sutherland's Law

$$\mu(T) = \frac{1.462 \times 10^{-6} T^{3/2}}{T + 112} \tag{2.6}$$

The freestream velocity can be expressed in terms of the freestream Mach number and sonic speed as

$$V = Ma \tag{2.7}$$

The unit Reynolds number is

$$Re = \frac{PV}{\mu RT} \tag{2.8}$$

from the perfect gas assumption. The dynamic pressure is

$$q = \frac{1}{2}\gamma M^2 P \tag{2.9}$$

which is used to obtain the aerodynamic coefficients of lift and drag.

Some example data of the pressure and temperature during a test run can be seen in Fig. 2.9. The total pressure and local temperature display the steady flow conditions between 0.18 s and 0.26 s. After 0.26 s, the unstart process begins, marking the end of the steady flow conditions in the test section.

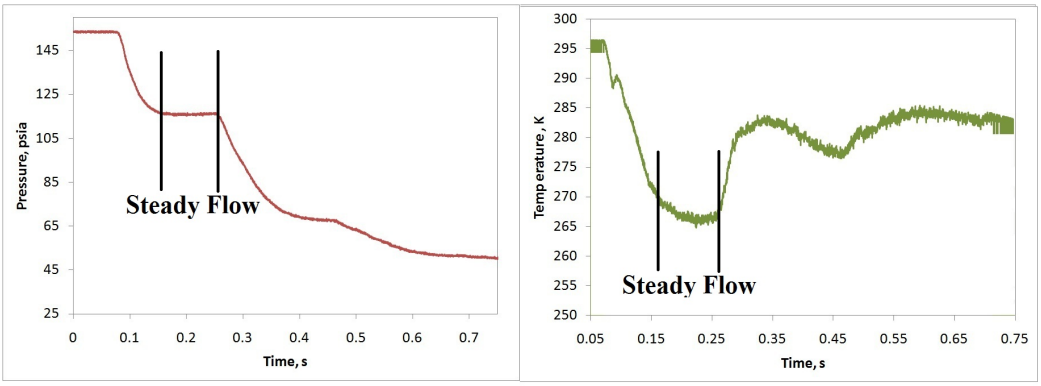

Figure 2.9. Example data of the total pressure and local temperature during a test run.

The test section pressure is displayed in Fig. 2.10, along with the Mach number and Reynolds number during the steady flow conditions. Before 0.15 s, the observation of the starting process can be seen. The Mach and Reynolds numbers increase to a steady value while the pressure and temperature remain constant during the same time period.

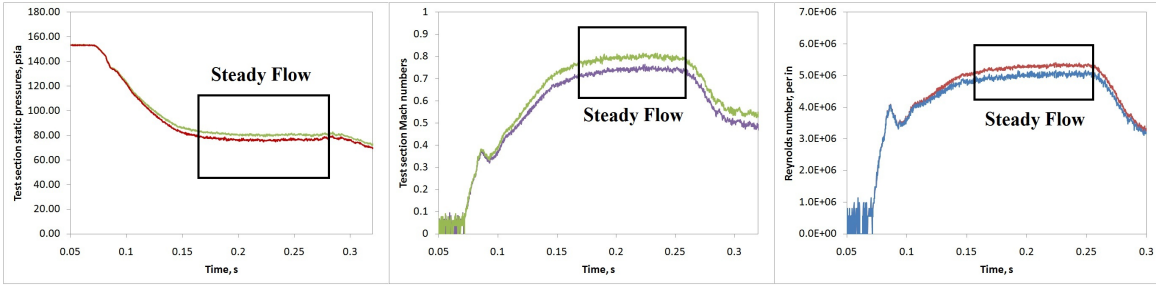

Figure 2.10. Example data of the test section pressure, and the calculated Mach and Reynolds numbers during a test run.

2.4 The Force Balance and the Model

Many types of force balances are available for use in wind tunnels, including pyramidal, sting, and sidewall. A pyramidal force balance is an example of an external balance, using struts that protrude from the wall of the wind tunnel since they are outside of the test section. However, sting and sidewall force balances are mounted within the wind tunnel and are examples of internal force balances. Tedious measurements and calculations are necessary to find the resolving center for pyramidal balances as well as drag and flow interferences with the support. Drag interferences also need to be considered for the sting mount due to the large support behind the model. Sting and sidewall balances require different calibration procedures since it is attached to the tunnel and interferes with measurement data.

These procedures and calculations are needed to get the true values of the aerodynamic forces. The values obtained from the strain gages need correction due the interaction forces created within the balance when in use. Therefore interaction matrices are necessary to single out the values of each force and moment. For the calibration and experimentation presented, an internal, sidewall force balance is used [19]. The use of sidewall balances is rare for Ludwieg tube tunnels, but the need to measure forces from a wall mounted model and the potential for testing a variety of models were appealing.

Table 2.2. Maximum loads for the force balance.

Component	**Max Load**
Normal Force (NF)	500 lbf
Rolling Moment (MX)	1000 lbf·in.
Chord Force (CF)	75 lbf
Yawing Moment (MZ)	150 lbf·in.
Pitching Moment (PM)	140 lbf·in.

The sidewall force balance for the UTA Ludwieg tube is a five-component balance, measuring the normal force (NF), the chord force (CF), the rolling moment (MX), the yawing moment (MZ), and the pitching moment (PM) using internal strain gages. The maximum loading values for each component can be seen in Table 2.2. Figures 2.11 and 2.12 shows the force balance and its configuration of the strain gages. It was purchased in 1989 from Modern Machine & Tool Company, Inc. in Newport News, Virginia, and custom-made for the UTA Ludwieg tube transonic tunnel. The balance is mounted to the tunnel test section using a side access port. It was last calibrated in 1991 using an obsolete PSP data acquisition system, so new technology and recalibration are necessary to achieve accurate measurements [14, 20]. With the

assistance of new programs and faster computer processors, the effect of dynamic loading can be understood and eliminated from the measurements.

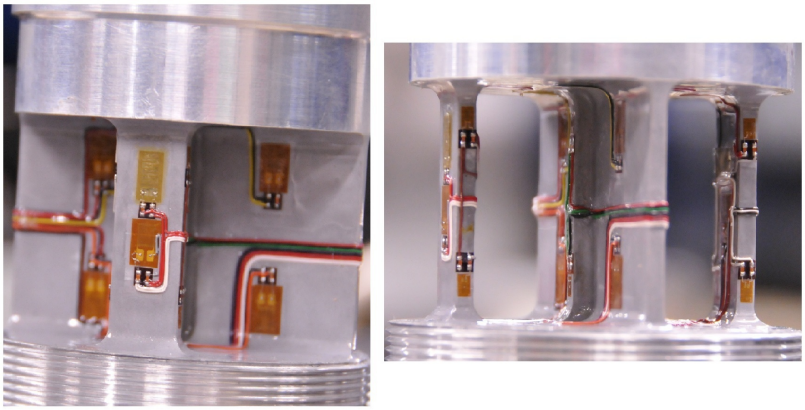

Figure 2.11. Photo of the force balance.

In [20], which is the original calibration report, information on all the strain gage bridges, raw data collected, and the process for obtaining the component measurements can be found. The *NF* and *MX* components are found from combining bridges R1 and R2, whereas *CF*, *MZ*, and *PM* components are directly found from bridges R3, R4, and R5, respectively, see Table 2.3. The bridge resistance is 350 Ω for all except R5, which is 700 Ω. An excitation voltage of 5 V is used for the old calibration, so for comparison purposes 5 V is also used for the current recalibration process. The offset of the load measurements is taken as the average of the data points for the first 0.05 s for each strain bridge. A schematic of the components discussed can be seen in Fig. 2.13.

Based on the configuration of the balance, the moments are taken at a specific position that depends on the orientation of a model to the balance. For airfoils, the most widely used positions for taking moments are the leading edge and the quarter-chord. If the model is not aligned with the pitching axis of the balance, the parallel

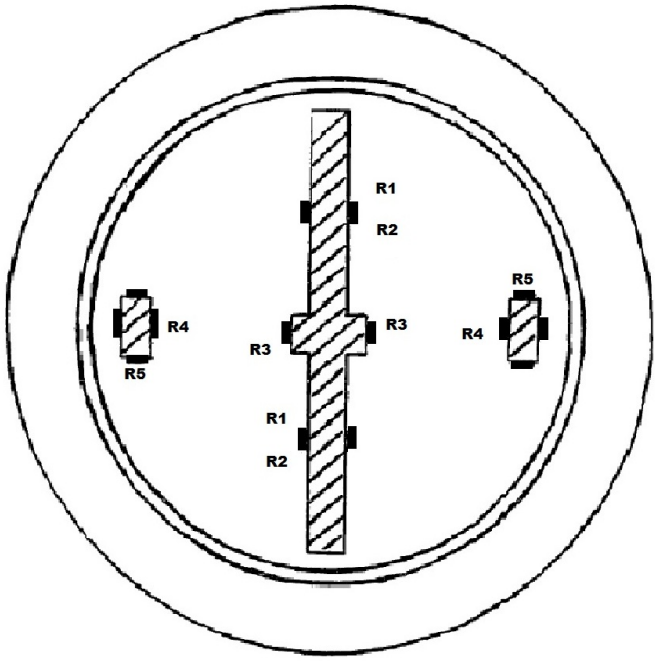

Figure 2.12. Strain gage configuration of the force balance.

axis theorem[1] should be used, knowing the distance r between the moment arms. Fortunately, the pitching axis of the balance is in line with the airfoil chosen[2] at the quarter-chord position. For a symmetric airfoil such as the one selected, the quarter-chord position is also the aerodynamic center. Therefore, it is not necessary to use the parallel-axis theorem for the moments in this case.

Using the force measurements from a run, the aerodynamic coefficients can be found at different angles of attack (α). The coefficient of lift (C_L), the coefficient of

[1] $I_{x1} = I_{x2} + Ar^2$

[2] NACA 0012 airfoil.

Table 2.3. Components found from the labeled bridges.

Component	Related Bridge
Normal Force (NF)	R2–R1
Rolling Moment (MX)	R2+R1
Chord Force (CF)	R3
Yawing Moment (MZ)	R4
Pitching Moment (PM)	R5

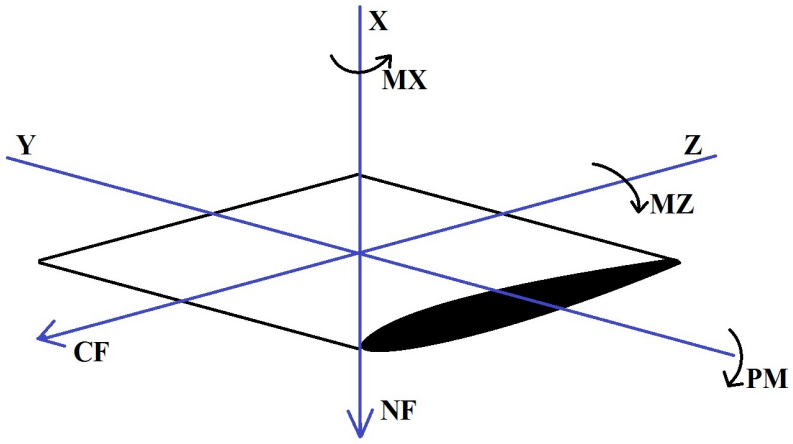

Figure 2.13. Schematic of the measured loads on a model by the force balance.

drag (C_D), the normal force coefficient (C_N), and the axial force coefficient (C_A) are found from the normal force and chord force by[3]

$$C_L = \frac{NF}{qS}\cos(\alpha) - \frac{CF}{qS}\sin(\alpha) \tag{2.10a}$$

$$C_D = \frac{NF}{qS}\sin(\alpha) + \frac{CF}{qS}\cos(\alpha) \tag{2.10b}$$

$$C_N = \frac{NF}{qS} \tag{2.10c}$$

$$C_A = \frac{CF}{qS} \tag{2.10d}$$

where

- NF = normal force (lbf)

[3] [3].

- CF = chord force (lbf)
- q = dynamic pressure (psia)
- S = planform area (in^2)
- α = angle of attack (deg, [°])

The lift-to-drag ratio L/D is defined as

$$L/D \equiv \frac{C_L}{C_D} \tag{2.11}$$

The moment coefficient C_M is found in a similar way:

$$C_M = \frac{PM}{qSc} \tag{2.12}$$

where c is the chord length (in.).

The process for static calibration is discussed in detail in Chap. 3, going over how the null of each test was determined, finding the sensitivity constants for each component, and separating the interactions between all of the components. This involves 13 nonlinear equations that are arranged in a 5×13 matrix that is used to find the true value of the components [20].

The model used for the calibration is a NACA 0012 airfoil (Fig. 2.14), which is symmetric, and has a chord length of 51 mm (2.0 in.) and a span of 109.2 mm (4.3 in.). The leading edge radius is 0.805 mm (0.0317 in.), and the curved tip has an area of 45.1 mm^2 (0.0699 in^2). Information on the thickness of the airfoil can be found in Table 2.4. From this information, the planform area was calculated to be 5570.96 mm^2 (8.635 in^2). This airfoil was chosen because of the historic data that are available for comparison.

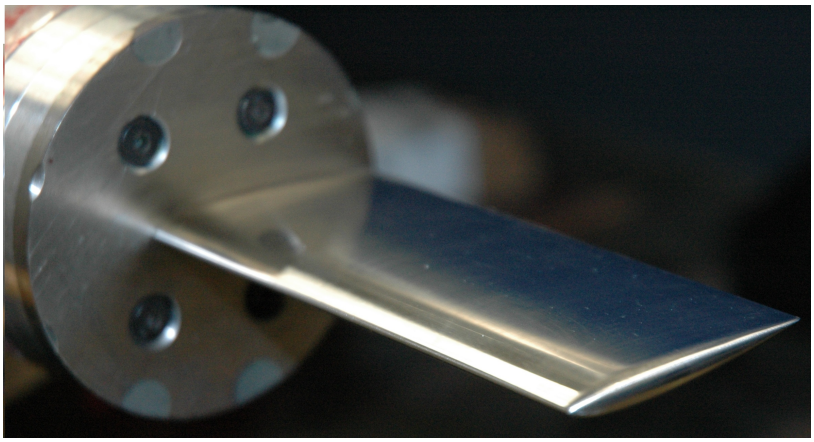

Figure 2.14. NACA 0012 airfoil model used for calibration process.

Table 2.4. Thickness variation of the NACA 0012 model.

Chordwise Position [in.]	**Thickness at Chord Point [in.]**
0.000	—
0.010	—
0.025	0.0758
0.050	0.1046
0.100	0.1422
0.150	0.1680
0.200	0.1873
0.300	0.2138
0.400	0.2295
0.500	0.2376
0.600	0.2401
0.800	0.2321
1.000	0.2118
1.200	0.1825
1.400	0.1466
1.600	0.1049
1.800	0.0579
1.900	0.0323
2.000	0.0050

CHAPTER 3

STATIC CALIBRATION

3.1 Introduction

The outdated calibration, as well as the disuse of the tunnel for research, necessitated that the force balance be recalibrated. Since the voltage readings are not directly related to the forces and moments acting on the balance, certain procedures and calculations are necessary to remove the interactions between the components and single out each component's true measurement (see §3.2). After multiple test runs and data analysis using the previous balance matrix, the measurement results found did not appear to be valid. This unsatisfactory situation led to the decision to recalibrate the force balance as well as to determine if a dynamic calibration is necessary.

3.2 Determining Force Measurements

In order to determine the force and moment measurements, the raw data need to be analyzed to remove the interaction forces that each of the strain gages create on one another. Referring to Table 2.3, the values for each voltage measurement θ are

multiplied by a sensitivity constant S to obtain force and moment units. The forces and moments can be written as elements of a vector $\vec{F}^{[0]}$, namely,

$$\vec{F}^{[0]} = \begin{bmatrix} \theta_{NF} & \theta_{MX} & \theta_{CF} & \theta_{MZ} & \theta_{PM} \end{bmatrix} \begin{bmatrix} S_{NF} \\ S_{MX} \\ S_{CF} \\ S_{MZ} \\ S_{PM} \end{bmatrix} \tag{3.1}$$

The 5×13 balance matrix $\mathbf{M}$ that contains the interaction values found from the calibration process relating the five force and moment components to the 13 interaction functions. The balance matrix is constant for any loading subjected to the force balance. The nonlinear interaction functions are related to the position of the static loadings used during calibration. The interaction equations and results can be found in App. A.2, while the balance matrix is found in App. A.3.

To obtain the corrected force measurements, the balance matrix is multiplied by the interaction vector $\vec{X}^{[i]}$, which contains the 13 interaction coefficients that are independent to each reading obtained by the force balance. Subtracting this from $\vec{F}^{[0]}$ provides a new force vector array $\vec{F}^{[i+1]}$. The new force vector values are then used in $\vec{X}^{[i]}$ to obtain another force vector $\vec{F}^{[i+2]}$:

$$\vec{F}^{[i+1]} = \vec{F}^{[0]} - \mathbf{M}^T \cdot \vec{X}^{[i]} \tag{3.2}$$

This process is iterated until the values of each measurement converge to their respective values, which occurs in approximately 15 iterations.

So how are the interactions, sensitivity constants, and the balance matrix determined? In order to find these values, known loads need to be applied to the force balance in precise locations. The strain gages are very sensitive, so any changes to the apparatus used will alter the measurements. For this reason, a nulling procedure was used, where zero load runs were conducted to remove the offset created by the setup. This was accomplished by attaching the necessary components for applying a load while reading zero load on the digital scale, namely an American Weigh TL-440 with a resolution of 0.5 lbf and a maximum capacity of 440 lbf.

3.3 Calibration Setup and Procedures

The balance was purchased with a calibration set that included a basket and a set of weights. The only things left behind from that set were the two attachments for the force balance. The weight set and basket are no longer available. The attachment for loading (Fig. 3.1) is precisely manufactured in order to focus on one or two components at a time.

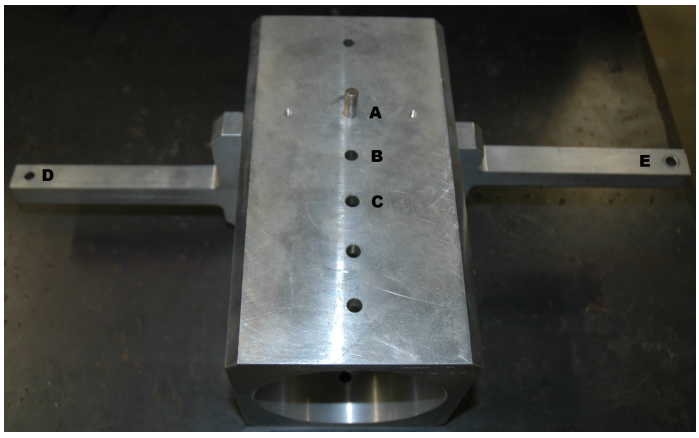

Figure 3.1. The calibration attachment necessary for static calibration with loading points labeled.

The pin in the center of the calibration piece (A) was used to measure the normal force or the chord force, depending on the axis, to give measurements without creating moments. The holes on the centerline are one (B) and two (C) inches from the center which allow for known applied moments. The arms on the sides create the pitching moment (D and E).

As seen in Fig. 3.2, the back end of the force balance is attached to an aluminum block. The block is held in place by the setup on the table which allows the balance to be extended over the edge of the table. The calibration apparatus is attached to the front, which allows the loads to be applied.

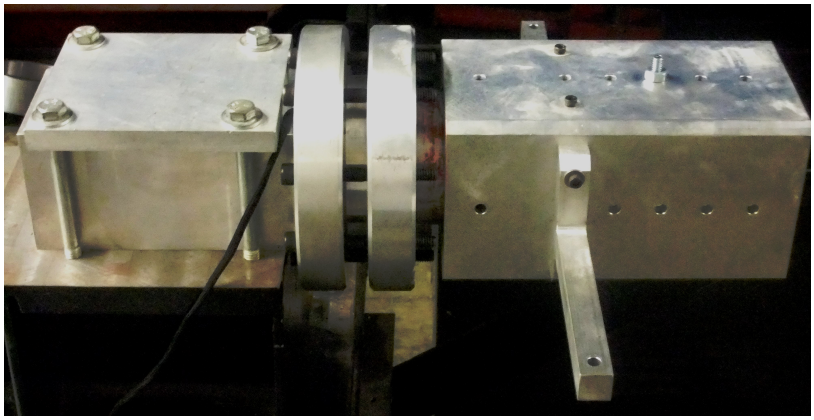

Figure 3.2. The calibration attachments on the force balance for static loading.

Since the weights were missing, a plate with eyebolts arranged in the same locations as the calibration attachment was designed and manufactured. The plate (Fig. 3.3) was installed on the floor directly beneath the calibration setup. Using another eyebolt, going through the attachment for stability, as well as a turnbuckle, a digital scale with a half-pound resolution, and a chain, connected the plate to the force balance calibration setup.

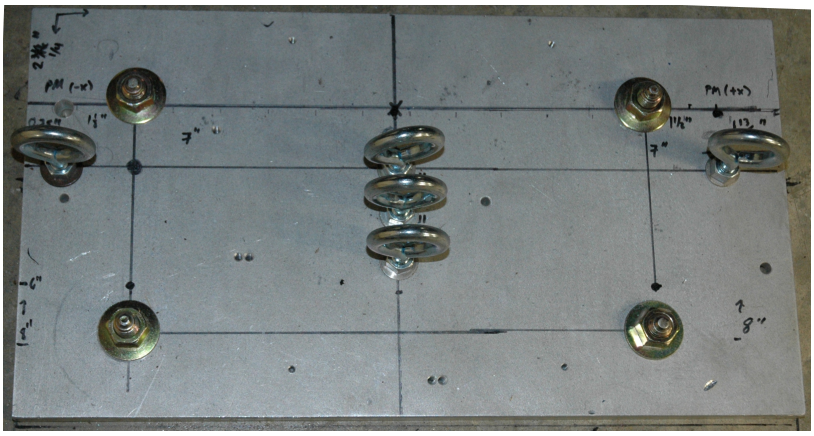

Figure 3.3. The plate that was manufactured for applying the static loads to the force balance.

After the setup was ready, the program recorded the readings as the zero load, so as to properly determine the measurements associated with the strain gage readings. The turnbuckle increased the applied load on the balance, which was read on the digital scale. The loads were applied in approximately equal increments up to the maximum value allowed by the strain gage or the instrumentation.

The locations of the loads applied were labeled according to the old calibration data, as seen in Fig. 3.1, and are explained in Table 3.1. The *NF* plane measures the normal force, moment about the X-axis, and the pitching moment. The *CF* plane measures the chord force and the moment about the Z-axis. The loading was applied to the positive and negative planes of each, where a (1) after a label indicates negative plane loading; e.g., point A1 is the negative plane loading at the center for the specified plane.

Table 3.1. Labels of the positions of loading points on calibration attachment.

Load Point	**Position**	**Remarks**
A	Center of Plane	No moment created
B	1 inch ahead of center	moment equals force
C	2 inches ahead of center	moment equals twice the force
D	Left pitching moment	*NF* plane only
E	Right pitching moment	*NF* plane only

3.4 Data Processing & Analysis

3.4.1 Determining the Sensitivity Constants

Static calibration data were obtained at a sampling frequency of 1600 Hz for one second since a large sample rate was not necessary for a steady, known load. After acquiring the data for each offset and load applied, the average and standard deviation for every 100 samples of each bridge were determined. The averages were examined to ensure that the applied force was constant. The voltages were then converted to mV for comparison with the previous calibration and recorded. The R1 and R2 bridges were combined to obtain the appropriate *NF* and *MX* measurements, while the *CF*, *MZ*, and *PM* measurements were directly related to their associated bridges. The data from load point A and A1 on the *NF* plane at 100 lbf can be seen below.

Table 3.2. Raw data processing from load point A of the *NF* plane at 100 lbf.

	R1 (V)	**R2 (V)**	**R3 (V)**	**R4 (V)**	**R5 (V)**
AVG	6.0434E–04	7.6521E–04	–1.4527E–05	2.3497E–05	–2.8320E–04
Std Dev	3.9065E–05	3.8840E–05	3.9648E–05	4.1681E–05	7.9479E–05
	***NF* (mV)**	***MX* (mV)**	***CF* (mV)**	***MZ* (mV)**	***PM* (mV)**
	0.16086	1.36955	–0.01453	0.02350	–0.28320

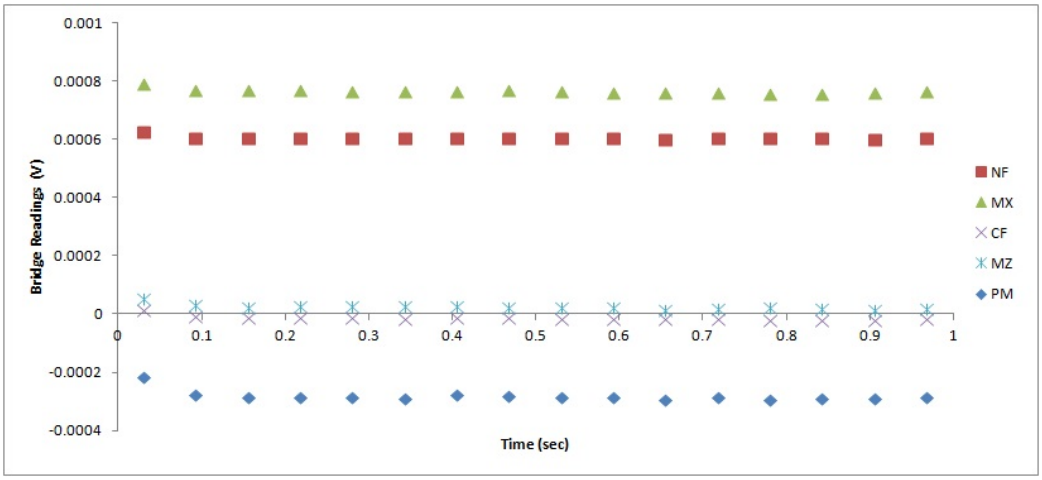

Figure 3.4. Graph of the bridge measurements for loading 100 lbf on load point A of the *NF* plane.

This was done for each applied load on each loading point. Table 3.3 shows the resulting voltages for the measurements of each applied load on point A of the *NF* plane. Afterwards, the data for the bridge of interest for each load point was plotted in order to find the sensitivity constant, as seen for load point A (*NF* component) of the *NF* plane in Fig. 3.5. The sensitivity data for the other force measurements can be found in App. A.1. The constants found from the positive and negative planes were averaged together for the best results in testing.

Table 3.3. Raw data at load point A of *NF* plane for static calibration.

Load (lbf)	***NF* (mV)**	***MX* (mV)**	***CF* (mV)**	***MZ* (mV)**	***PM* (mV)**
0	0.00940	0.16277	0.00613	0.03924	–0.12666
100	0.16086	1.36955	–0.01453	0.02349	–0.28320
200	0.31897	2.58371	–0.03601	0.01132	–0.40682
298	0.47985	3.76556	–0.04819	–0.00003	–0.49988
398	0.61601	4.98012	–0.05886	–0.01105	–0.55158

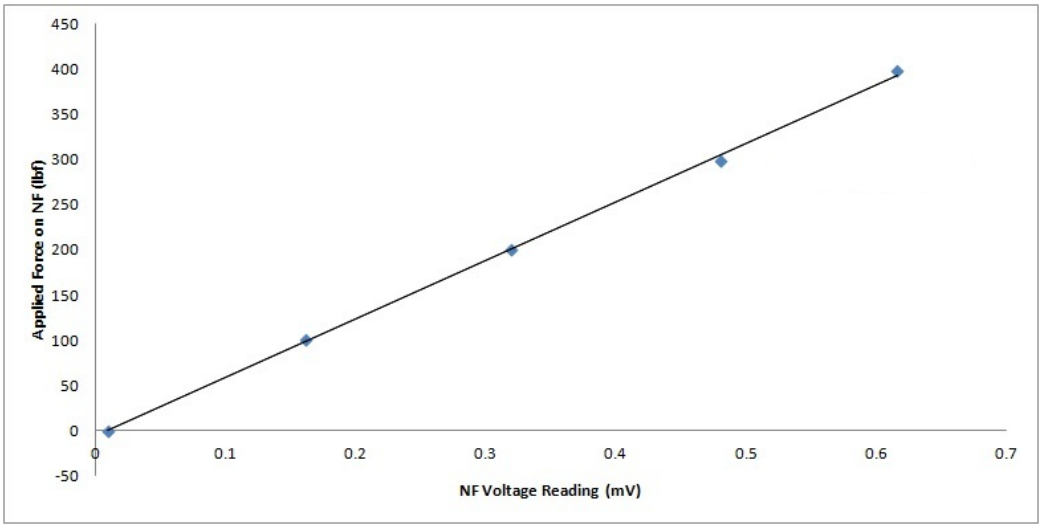

Figure 3.5. From the trendline equation, $y = 648.27x - -6.3143$, $R^2 = 0.999$, the sensitivity constant can be found from the load data for point A of the *NF* plane.

The sensitivity constants that were found are shown in Table 3.4, along with the previous sensitivity constants. Notice that the constants for *NF*, *CF*,and *PM* are relatively close to their previous values. However, the constants for *MX* and *MZ* are further from their previous value. The applied forces were similar to those of the previous calibration, so the decision was made to continue with this data since the important components were *NF*, *CF*, and *PM*.

Table 3.4. Current and previous sensitivity constants of the components of the force balance.

Component	**Current S Constant**	**Previous S Constant**	
NF	642.46222	630.51702	(lbf/mV)
MX	131.94153	147.95088	(lbf·in./mV)
CF	11.385700	11.79616	(lbf/mV)
MZ	119.27487	137.74105	(lbf·in./mV)
PM	26.039825	24.88447	(lbf·in./mV)

The sensitivity constants appear to match closely with the previous values. The departure in the manufacturer's constant was less than 5% for the three components of interest: *NF*, *CF*, and *PM*. The departure in *MX* is about 11%, while for *MZ* the departure is 13.4%.

3.4.2 Determining the Interaction Coefficients

After finding the sensitivity constants, the largest applied load for each component was used to determine the balance matrix. Using the strain gage voltages obtained for both the positive and negative planes and accounting for the calibration setup, voltages of each component were acquired. For the load points A (positive plane) and A1 (negative plane) of the *NF* plane, the maximum load amounts and their corresponding strain gage readings for each component are seen in Table 3.5. For the maximum loads used for each load point during the static calibration along with the measurements from each component, see App. A.2.

Table 3.5. Loading and raw strain gage measurements for load points A and A1 of the *NF* plane.

	Load Pt	***NF***	***MX***	***CF***	***MZ***	***PM***
Load (lbf)	(+) plane	398.0	0.0	0.0	0.0	0.0
Measurement (mV)	A	0.606615	4.817348	–0.064993	–0.050290	–0.424923
Load (lbf)	(–) plane	–399.5	0.0	0.0	0.0	0.0
Measurement (mV)	A1	–0.630346	–4.995186	0.027586	0.108115	–0.045612

Notice that the measurements do not go to zero. Thus it is necessary to reduce the influence that one component reading has on the rest, which is accomplished with the interaction equations. Using the measurements, a vector of 13 values based on the

nonlinear equations provided by the calibration report [20] determines the interaction coefficients. The equations based on the NF plane are

$$NF = \frac{A - A1}{2} \tag{3.3a}$$

$$NF^2 = \frac{A + A1}{2} \tag{3.3b}$$

$$MX = (C - C1) - (B - B1) \tag{3.3c}$$

$$MX^2 = (C + C1) - 2\,(B + B1) + (A + A1) \tag{3.3d}$$

$$NF \times MX = 2\,(B + B1) - 0.5\,(C + C1) - 1.5\,(A + A1) \tag{3.3e}$$

$$PM = \frac{(D - D1) - (E - E1)}{4} \tag{3.3f}$$

$$PM^2 = \frac{(D + D1) + (E + E1)}{4} \tag{3.3g}$$

$$NF \times PM = 6.25\,[(D - E) + (D1 - E1)] \tag{3.3h}$$

while those based on the CF plane are

$$CF = \frac{A - A1}{2} \tag{3.4a}$$

$$CF^2 = \frac{A + A1}{2} \tag{3.4b}$$

$$MZ = (C - C1) - (B - B1) \tag{3.4c}$$

$$MZ^2 = (C + C1) - 2\,(B + B1) + (A + A1) \tag{3.4d}$$

$$CF \times MZ = 2\,(B + B1) - 0.5\,(C + C1) - 1.5\,(A + A1) \tag{3.4e}$$

For the *NF* component, the interaction vector of coefficients is shown in Table 3.6. This vector utilizes the strain gage measurements from each load point for both positive and negative *NF* and *CF* planes in Eqns. (3.3) and (3.4). The complete table of all interaction coefficients for each component can be found in App. A.2.

Table 3.6. Interaction vector of coefficients for the *NF* component to calculate the balance matrix.

Component	**NF interaction (mV)**
NF	0.618480
NF^2	–0.011866
MX	–0.110106
MX^2	0.022231
$NF \times MX$	–0.017393
PM	–0.021534
PM^2	0.00631
$NF \times PM$	0.003661
CF	–0.027622
CF^2	0.005976
MZ	0.000705
MZ^2	0.058386
$CF \times MZ$	–0.081259

3.4.3 Determining the Balance Matrix

The balance matrix can be determined using the interaction coefficients and strain gage measurements with their respective sensitivity constants. The balance matrix column for the *NF* component using its interaction vector (Table 3.6) is

$$B_{NF} = \frac{(V_{NF} S_{NF})}{(I_{nf-nf} S_{NF})} \tag{3.5a}$$

$$B_{NF^2} = \frac{(V_{NF^2} S_{NF})}{(I_{nf-nf} S_{NF})\,(I_{nf-nf} S_{NF})} \tag{3.5b}$$

$$B_{MX} = \frac{(V_{MX} S_{NF})}{(I_{mx-mx} S_{MX})} \tag{3.5c}$$

$$B_{MX^2} = \frac{(V_{MX^2} S_{NF})}{(I_{mx-mx} S_{MX})\,(I_{mx-mx} S_{MX})} \tag{3.5d}$$

$$B_{NF\times MX} = \frac{(V_{NF*MX} S_{NF})}{(I_{nf-nf} S_{NF})\,(I_{mx-mx} S_{MX})} \tag{3.5e}$$

$$B_{PM} = \frac{(V_{PM} S_{NF})}{(I_{pm-pm} S_{PM})} \tag{3.5f}$$

$$B_{PM^2} = \frac{(V_{PM^2} S_{NF})}{(I_{pm-pm} S_{PM})\,(I_{pm-pm} S_{PM})} \tag{3.5g}$$

$$B_{NF\times PM} = \frac{(V_{NF*PM} S_{NF})}{(I_{nf-nf} S_{NF})\,(I_{pm-pm} S_{PM})} \tag{3.5h}$$

$$B_{CF} = \frac{(V_{CF} S_{NF})}{(I_{cf-cf} S_{CF})} \tag{3.5i}$$

$$B_{CF^2} = \frac{(V_{CF^2} S_{NF})}{(I_{cf-cf} S_{CF})\,(I_{cf-cf} S_{CF})} \tag{3.5j}$$

$$B_{MZ} = \frac{(V_{MZ} S_{NF})}{(I_{mz-mz} S_{MZ})} \tag{3.5k}$$

$$B_{MZ^2} = \frac{(V_{MZ^2} S_{NF})}{(I_{mz-mz} S_{MZ})\,(I_{mz-mz} S_{MZ})} \tag{3.5l}$$

$$B_{CF\times MZ} = \frac{(V_{CF*MZ} S_{NF})}{(I_{cf-cf} S_{CF})\,(I_{mz-mz} S_{MZ})} \tag{3.5m}$$

$$\tag{3.5n}$$

where

- V_{XX} = corresponding value in Table 3.6
- S_{XX} = component sensitivity constant (Table 3.4)
- I_{xx-xx} = interaction coefficient of the component with itself; e.g., row 1 of Table 3.6 where $I_{nf-nf} = 0.618480$

- B_{XX} = value in the balance matrix corresponding to that interaction with the NF component

The corresponding values from Eqn. (3.5) for the NF component are in Table 3.7.

Table 3.7. NF component column of the balance matrix.

	NF
NF	0.00000E+00
NF^2	–4.82826E-05
MX	–1.01484E-01
MX^2	2.93950E-05
$NF{\times}MX$	–4.03456E-05
PM	–9.81294E-02
PM^2	2.03841E-04
$NF{\times}PM$	4.19863E-05
CF	–2.37241E-01
CF^2	6.86131E-04
MZ	4.53346E-03
MZ^2	3.76040E-03
$CF{\times}MZ$	–6.98772E-03

The entire balance matrix $\mathbf{M}$ and the interaction vector $\vec{X}^{[i]}$ can be seen in App. A.3. For the cells that signify the component interacting with itself in the balance matrix (e.g., row 1 of Table 3.7), the value should go to zero even though the arithmetic says a value of unity (1.00). This is necessary in order to use the vector-matrix dot product. A more detailed version of Eqn. (3.2) can be seen in App. A.4.

3.5 Accuracy Analysis

After calculating $\mathbf{M}$, an accuracy check was completed to ensure the matrix and Eqn. (3.2) produced accurate results. Since using the equation is an iterative

process, a Matlab program (App. C) was created to decrease processing time. Using the raw data gathered from each test, the corrected measurements were obtained and compared to the known forces and moments. Since 1600 samples were taken, each raw data line was used in the equation and finally averaged.

Table 3.8. Accuracy check of the *NF* component on loading point A for the *NF* plane.

A	*NF*	*MX*	*CF*	*MZ*	*PM*
Reading(mV)	0.607	4.817	–0.065	–0.050	–0.425
App. Load (lbf)	398.0	0.0	0.0	0.0	0.0
Uncorr. Load	389.727	635.608	–0.740	–4.224	–11.029
Avg from Matlab	397.3024	0.0762	8.04E–04	0.0198	–0.0151
Difference	0.69760	–0.07620	–0.00080	–0.01980	–0.01510
%Error (Full Load)	0.14%	0.0076%	0.0011%	0.013%	0.011%

The "Uncorrected Load" was found from multiplying the raw averaged data measurement to the component's sensitivity constant. The "Difference" pertains to the measurement difference between the applied load and the value from the Matlab code. The "Percent Error" was determined by taking the "Difference" and dividing by the full load capability of the component. The accuracy check for the other load points can be found in App. A.5.

3.6 Test Results

After using the averaged values of the components to find the balance matrix, it was determined that a low-pass filter would assist in reducing some of the high frequency noise associated with test runs. Using a sampling frequency of 5000 Hz, two runs were conducted at approximately the same test conditions, with an α of

$\pm 3°$. The filter was set at 300 Hz, shown in red on the graphs, and applied after the iterative equation, Eqn. (3.2).

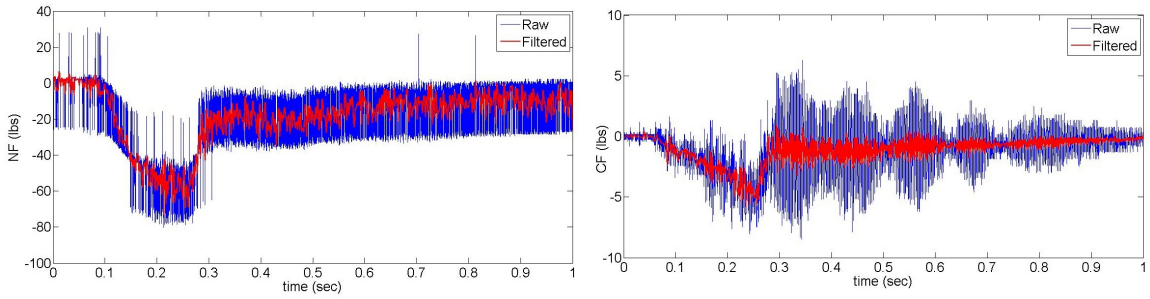

Figure 3.6. *NF* and CF readings from the balance at a $\alpha = 3°$.

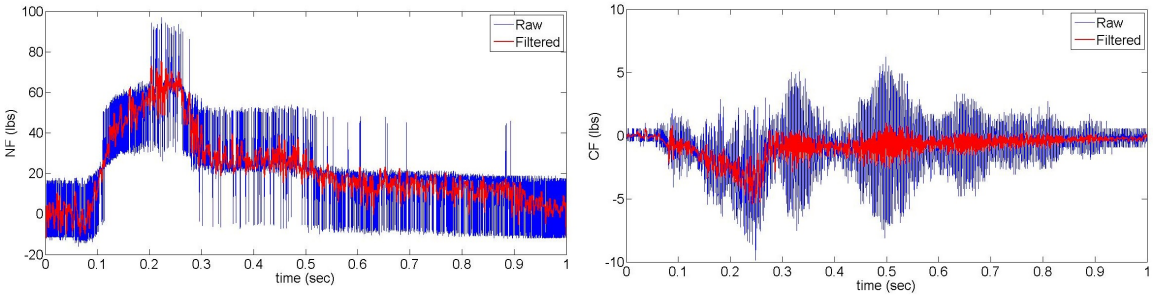

Figure 3.7. *NF* and CF readings from the balance at a $\alpha = -3°$.

Notice in Figs. 3.6 and 3.7 that the chord force does not become steady. It is known that there is a small gap between the wall of the tunnel and the base of the airfoil which allows the model to flex under the loads created by the tunnel. This creates the gradual increase in the chord force measurement. Also, the orientation of the balance creates the appearance of a negative force value. This is due to the coordinate system selected by the manufacturer. The signs are consistent with actual

measurements, concluding that the original orientation given by the manufacturer is opposite of the true orientation (see Fig. 2.13).

The two tests were conducted at Mach 0.76 with a Reynolds number of 5.3 million and a dynamic pressure of 218.5 kPa (31.1 psia). From the results of these two test runs, the steady flow time was found to be between 0.2 s and 0.25 s due to the noticeable change in the force measurements during the steady flow time frame. Table 3.9 shows the data from each run. The main cause for the difference in the tests is possibly due to a slight difference in the test conditions, specifically Mach number and Reynolds number, and the uncertainty in α.

Table 3.9. Test data after static calibration for α of 3° and $-3°$ using the time frame 0.2 s – 0.25 s and the orientation.

	$\alpha = 3°$	$\alpha = -3°$
NF (lbf)	–56.4843	61.2089
CF (lbf)	–4.1520	–3.3691
PM (lbf-in)	6.2600	–8.0856
c_l	0.20977	–0.22715
c_d	0.02651	0.02447
c_m	–0.01168	0.01506
L/D	7.91123	–9.27972

According to the data from Mineck and Hartwich [6], at approximately $\alpha = 3°$, $M_\infty = 0.76$, $Re = 236$ million/m (6.0 million/inch) and the value of $c_l = 0.4194$, $c_d = 0.0220$, and $c_m = 0.001$ for a NACA 0012 airfoil. The value of the present drag coefficient appears relatively close, however the lift and the moment coefficients do not appear to correlate well. There are multiple possibilities for this, including, but not limited to,

- comparing infinite and finite wing data

- test condition variation within the steady flow test time
- a low sampling frequency for data acquisition
- noise and interference of the signal due to vibrations and the acceleration of the wind tunnel during experiments
- incorrect timing of the plenum cutter with the sliding sleeve valve

The majority of these issues can be resolved by making adjustments to the experiments and using dynamic calibration on the force balance. By altering the time delay of the plenum cutter, a steadier flow regime can be achieved, allowing for a more constant Mach number, Reynolds number, and possibly force balance measurements. By accounting for dynamic calibration of the model and force balance, vibrations and interference within the measurements can be removed to provide truer force measurements.

CHAPTER 4

DYNAMIC CALIBRATION

4.1 Introduction

Dynamic calibration is necessary due to the interference created by stress waves within the model from suddenly applied loads. Since only a short period of quasi-steady flow conditions exist during any one test run, the balance will be subjected to extraneous inertia forces. Knowing the dynamics of the balance and model allows the history of the forces that are applied to be determined from the raw measurements [21]. The model and the balance can be considered to be a linear system based on the relationship between the voltage and the load (sensitivity constants) [21]. However, if a different model is used on the force balance, another dynamic calibration would need to be performed. If the output of the system is $y(t)$, which includes the developed interference within the model, and the applied load is $u(t)$, the relationship between them is the convolution integral

$$y(t) = \int_0^t g(t-\tau)u(\tau)\,\mathrm{d}\tau \tag{4.1}$$

where $g(t)$ is the impulse response function [22].

Different methods can be used to determine $g(t)$. For this calibration, a known impulse input $u(t)$ is applied to the balance and model while measuring the corresponding output $y(t)$. By taking the Laplace transform of Eqn. (4.1), the transfer function $G(s)$ can be found by

$$G(s) = \frac{Y(s)}{U(s)} \tag{4.2}$$

where $Y(s)$ and $U(s)$ are the transforms of $y(t)$ and $u(t)$, respectively [23]. Note that $G(s)$ never changes for a particular bridge circuit, so it is independent of the input. The inverse Laplace transform is then applied to $U(s)$ to yield the true input on the model and balance $u(t)$.

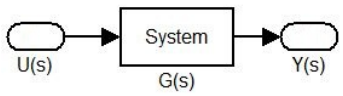

Figure 4.1. The measured output $Y(s)$ is found from an input $U(s)$.

According to Robinson [23], there are some constraints involved in order to deconvolve a signal properly. The most important is when a non-periodic signal is transformed into the frequency domain, generating errors within the signal due to Gibbs phenomenon "in the vicinity of a jump discontinuity" [24]. This phenomenon can be reduced by using low-pass filters. In this case, an impulse is used which has a low step value and reduces the possibility of this phenomenon further. Another constraint is that "the inverse FFT requires the entire time history to produce an accurate result" [23]. In other words, if the number of samples and sampling frequency during a test run were different from those used during the dynamic calibration process, this method would not suffice. The number of samples and sampling frequency must be the same between the calibration and the testing.

One common issue associated with deconvolution is numerical instability due to the presence of high frequencies. If the initial value of the physical response is close to zero, and since dividing by low values is in fact a large multiplier, noise and error can be greatly magnified. Due to this, instability occurs since each input sample is dependent on the previous value [23]. Stability of the process can be accomplished by reducing the noise, removing outliers, and filtering.

4.2 Calibration Method and Testing

For the dynamic calibration of this model and balance, a PCB 086C01 impulse force hammer is used to provide and measure the input. The input and output are measured by the "Transonic" LabView program. The hammer has a rubber tip attached to prevent damage to the model and balance during the testing. When using an impulse hammer to measure a pulse, consideration must be taken to ensure that low frequency noise does not interfere with the measured signals, including small DC offsets. In addition, better pulse calibration can be obtained if the hammer signal is zero when it is not in contact with the model since a non-zero signal over time can be integrated to seemingly significant values compared to a short contact period [25]. It should also be noted that the deconvolution process can yield poor results if multiple hammer pulses are measured during a single calibration test. An example of a good input impulse can be seen in Fig. 4.2. The impulse force generates a response from the component of interest at the time of impact, which is used to calculate the transfer function to eliminate the interference within the data.

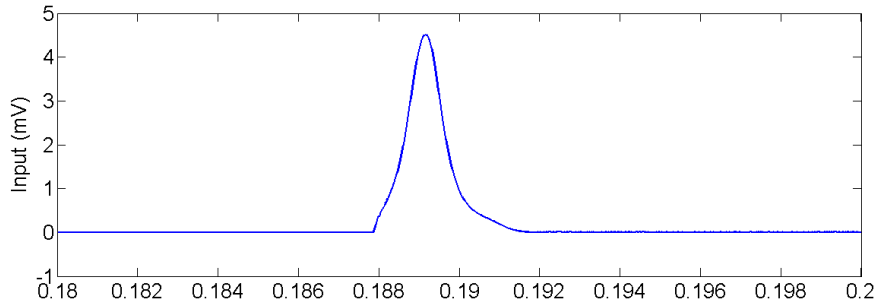

Figure 4.2. A measured input signal from the impulse force hammer.

The test setup is similar to that of the static calibration setup in that the force balance is mounted to a rigid table via an aluminum block attached to the back.

The NACA 0012 airfoil model is attached to the force balance instead of the static calibration apparatus, and the impulse hammer is used to excite the strain bridges within the balance. The applied impulse should have the same sign as the force that is measured by the bridges. For example, the hammer should strike the leading edge or trailing edge of the airfoil for the chord force and the top or bottom surface of the airfoil for the normal force.

Since this process requires equal samples and sampling rates between the experiments and the calibration testing, different sample rates were chosen in the event a different frequency was necessary for other measurements. The frequencies chosen were 5 kHz, 25 kHz, 50 kHz, and 80 kHz. The time frame chosen is one second, which is the same as a test run. Originally it was thought that 5 kHz would be sufficient for the calibration and test runs, but the stress wave speed in the stainless steel model is approximately 5190 m/s (17,027 ft/s) [26] and could possibly alias the true values due to the low sampling frequency. Therefore, the 50 kHz rate was used to acquire the dynamic calibration and test data for the remainder of the experiments. Comparisons were made to determine if significant changes occur in the data due to the sampling frequency.

4.3 Data Processing and Analysis

Assessments were conducted in order to record a pure impulse and the resulting influence on the force measurements. The calibration was conducted for the NF and CF components only. Calibration for the moments were not necessary for MX and MZ since they are not significantly important components when dealing with the present aerodynamic loads. The PM component could not be calibrated due to the uncertainty of the applied input moment.

A Matlab code was developed to analyze the dynamic calibration data, taking the data for the input and the output from an Excel file and Fourier transforming them from the time domain to the frequency domain. The input and the output were processed in mV to keep the transfer function $G(s)$ dimensionless. Two different cases were used: one to calculate $G(s)$ and one to confirm that the $G(s)$ is calculated correctly to eliminate the influence of vibrations and noise on the model. The best possible transform function is one that matches a second case, with known input and output, as close as possible.

For the *CF* component, the bridge signal is directly related to the force measurement so the relationship is linear. However, the input force was recorded as a positive number, while the output was negative. Therefore the inputs for calibration tests of the *CF* component were converted to negative values by multiplying the measurement by –1. At 50 kHz, the comparison of the transformed data of case 2 to the actual data of case 2 is seen in Fig. 4.3. Notice that the transformed data shown by the blue line almost matches the actual data shown by the red line, indicating that the transformation is good.

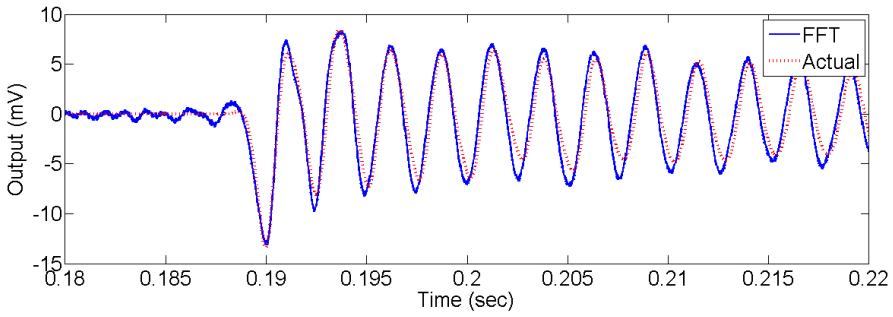

Figure 4.3. Transformed data versus actual data for *CF* component at 50 kHz.

The results of the other sampling rates are shown in App. B.2. At 5 kHz, the sampling frequency is too low to provide an accurate comparison of the transfer function and the actual output of the *CF* component. At 25 kHz and 80 kHz, the transfer function appears to be of good quality with only a couple of peaks that do not match properly.

The Matlab code that was developed for the dynamic calibration of the *CF* component can be found in App. B.1. It can be easily modified for the different sample frequencies by changing the files used and the row numbers in the Excel files.

The *NF* component was slightly different for the dynamic calibration since the measurement is the difference between two bridge signals, but the relationship is still linear. A larger input force was necessary to calculate an appropriate transfer function for the *NF* component since it is more sensitive to the strain measurements than the *CF* component. Figure 4.4 shows the comparison of the transformed data of case 2 (blue) and the actual data of case 2 (red) for a sampling frequency of 50 kHz. Appendix B.3 lists the Matlab code developed for the dynamic calibration of the *NF* component.

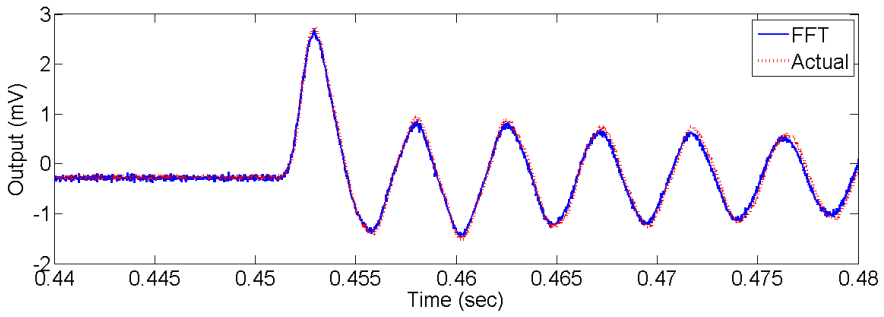

Figure 4.4. Transformed data versus actual data for *NF* component at 50 kHz.

The other sampling frequencies for the *NF* component can be seen in App. B.4. At 5 kHz the sampling frequency matches the first few peaks, but the transfer function begins to undervalue the actual value too quickly, in addition to some off-timing. At 25 kHz, the transfer function is leading the actual signal immediately after the input, so the transfer function is still not completely correct. At 80 kHz, the R1 bridge strain measurement immediately increases without an input, indicating that the sampling rate is possibly too high for the signal conditioner. Since the value of the *NF* component is dependent on the difference between R2 and R1, the transfer function is affected by this issue. Therefore, the transfer function for *NF* cannot be calculated at sampling rates that exceed the limits of the signal conditioners.

4.4 Results

After the transfer functions were determined for the *NF* and *CF* components, experiments at $\alpha = 0.1^\circ$ and 2.9° were conducted to determine the viability of the calibration. These tests had a sample frequency of 50 kHz with test conditions at approximately Mach 0.75, $Re_\infty = 5.1$ million, and $q_\infty = 204.1$ kPa (29.6 psia). The low-pass filter in the Matlab code was set at 300 Hz, showing the raw filtered data in blue on the graphs, while the filtered transformed data are shown in red for the two force components, *NF* and *CF*, as seen in Figs. 4.5 and 4.6.

For the experiment at $\alpha = 0.1^\circ$, the numeric results are shown in Table 4.1. Figures 4.5 and 4.6 show the comparison of force measurement data, where the *NF* component increases by 3.6 lbf, or 57%, and the *CF* component decreases by 1.263 lbf, or 29%.

The numeric results for the experiment at $\alpha = 2.9^\circ$ are shown in Table 4.2. Figures 4.8 and 4.9 show the difference in the force measurement data between the static calibration and dynamic calibration, while Fig. 4.10 shows the measured pitch-

Table 4.1. Test data comparing static to dynamic calibration for $\alpha = 0.1°$ using the time frame 0.18 – 0.25 s.

	Only Static Calib.	**With Dynamic Calib.**
NF (lbf)	–6.284	–9.884
CF (lbf)	–4.381	–3.117
PM (lbf·in.)	–0.092	–0.092
MX (lbf·in.)	–15.54	–15.54
MZ (lbf·in.)	–4.597	–4.597
C_L	0.0238	0.0375
C_D	0.0167	0.0119
C_M	0.00017	0.00017
L/D	1.43	3.15

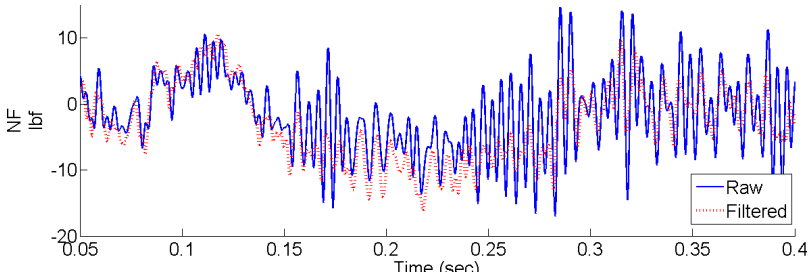

Figure 4.5. NF component at $\alpha = 0.1°$ showing raw data and calibrated data.

ing moment. For the chosen time frame, the NF component increases by 26.36 lbf or 50% while the CF component decreases by 1.173 lbf or 30%, significantly changing the C_L and C_D values.

The data from these two experiments are compared to those Mineck and Hartwich [6], seen in Table 4.3, taken at Mach 0.76 and $Re_\infty = 4.0$ million/inch for an infinite wing at $\alpha = 0.0°$ and $3.0°$. Since these data are for an infinite wing, there are some differences that are to be expected between the data sets.

The comparison for $\alpha = 2.9°$ shows that C_L is closer to Mineck and Hartwich's data with the dynamic calibration while C_D is further. This is due to the influence on C_D from the value of C_L, seen in Eqn. (2.10). It is expected that the values of

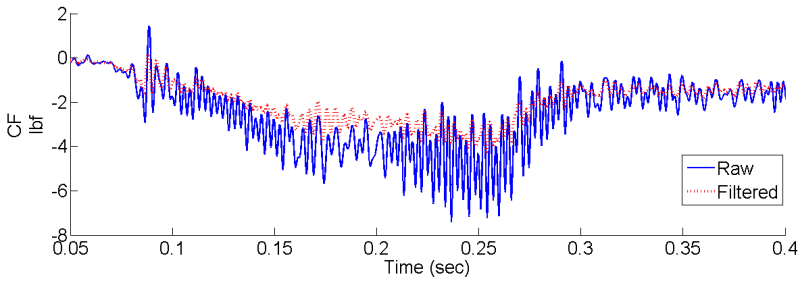

Figure 4.6. *CF* component at $\alpha = 0.1°$ showing raw data and calibrated data.

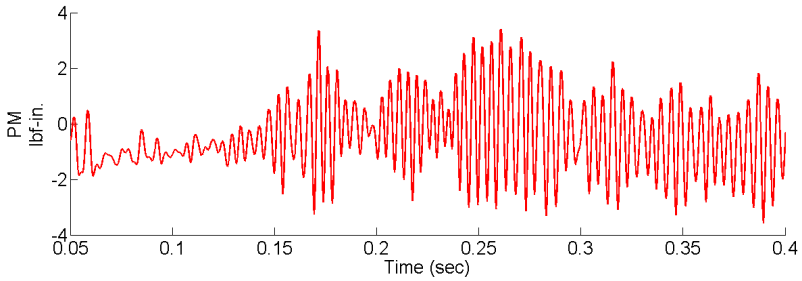

Figure 4.7. *PM* component at $\alpha = 0.1°$ showing the raw data.

the coefficients would act accordingly because of the finite wing geometry and the larger pressure loads exerted on the model during a test run. Another comparison is the L/D ratio, which appears to be within reason considering the slightly lower α, the differences in Mach and Reynolds numbers, and the change in data between infinite and finite wings due to the aerodynamics. For C_M, the experimental data are a magnitude higher likely because of the vortices created at the tip of a finite wing, considering the data from [6] is for an infinite wing.

At $\alpha = 0.1°$, the comparison to Mineck and Hartwich's data is reversed. The C_L from the experiment is higher with the dynamic calibration when compared to [6], but C_D goes lower, giving a better comparison for drag. The L/D ratio is slightly larger with the change in C_L, but this is expected with the slight difference in α as well as the test conditions. The C_M is now one order of magnitude lower due to the vortices on finite wings that are not found on infinite wings.

Table 4.2. Test data comparing static to dynamic calibration for $\alpha = 2.9°$ using the time frame 0.18 – 0.25 s.

	Only Static Calib.	**With Dynamic Calib.**
NF (lbf)	–51.843	–78.209
CF (lbf)	–3.9369	–2.7632
PM (lbf·in.)	6.1147	6.1147
MX (lbf·in.)	–147.82	–147.82
MZ (lbf·in.)	–5.573	–5.573
C_L	0.2016	0.3048
C_D	0.0256	0.0262
C_M	–0.0119	–0.0119
L/D	7.8687	11.6086

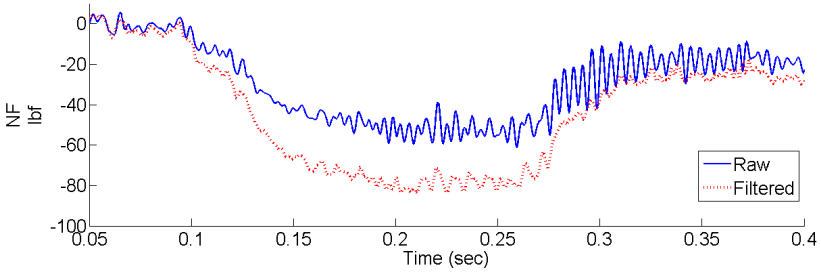

Figure 4.8. NF component at $\alpha = 2.9°$ showing raw data and calibrated data.

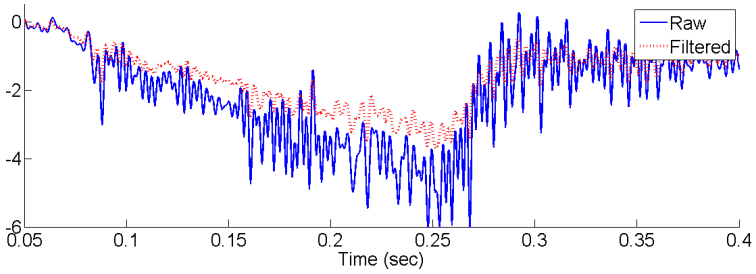

Figure 4.9. CF component at $\alpha = 2.9°$ showing raw data and calibrated data.

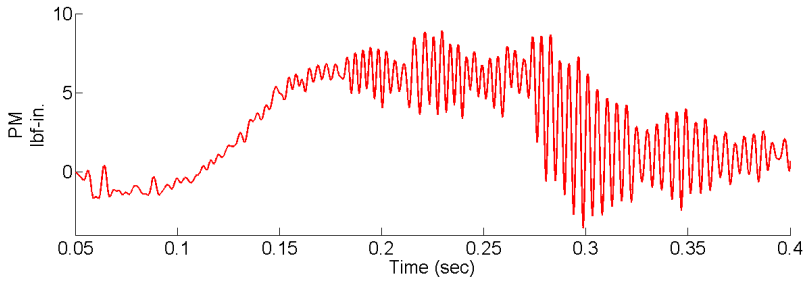

Figure 4.10. *PM* component at $\alpha = 2.9°$ showing the raw data.

Table 4.3. Data from Mineck and Hartwich [6] for $\alpha = 0.0°$ and $\alpha = 3.0°$ at Mach 0.76.

	$\alpha = 0.0°$	$\alpha = 3.0°$
C_L	0.0200	0.4194
C_D	0.0090	0.0230
L/D	2.2222	18.235
C_M	0.0010	0.0010

CHAPTER 5

DATA VALIDATION AND ERROR ANALYSIS

5.1 Introduction

After the calibration procedures were completed, a parametric study was performed to confirm that the force balance provides correct and accurate results. The comparison for the NACA 0012 wingtip is an infinite wing case performed by Mineck and Hartwich of NASA [6]. Differences between the experimental data and the published data are expected since the aerodynamic effects are different for a finite and an infinite wing. An error analysis was performed using a 95% confidence interval and the propogation of error equation to determine the uncertainty in the measured and calculated data.

5.2 Procedures and Calculations

The parametric study was performed at test conditions of Mach 0.75, a Reynolds number of 3 million, and the angle of attack α was varied in one degree increments from -4° to 7°. The sampling rate for the data acquisition was 50 kHz. The test conditions for [6] were Mach 0.76, Reynolds number at 4 million, and an α varying from 0° to 5°. Numeric values were not provided by Mineck and Hartwich, but inferred from the charts provided in the report. The information used from Mineck and Hartwich is provided in App. D.1. A direct comparison is not possible between these data sets but the overall trends should correspond. The aerodynamic coefficients were calculated in the same manner provided in §2.4.

5.3 Results and Comparison

Using a low-pass filter set at 100 Hz, the change in the *NF* component can be seen clearly in Fig. 5.1. Due to the orientation of the force balance, a negative α produce positive values and vice versa. The blue line denotes the raw data, meaning static calibration only, with the corresponding α in gray, while the red line indicates the dynamically calibrated data with α in black. As α departs from 0°, the difference between the static and dynamic calibration increases significantly.

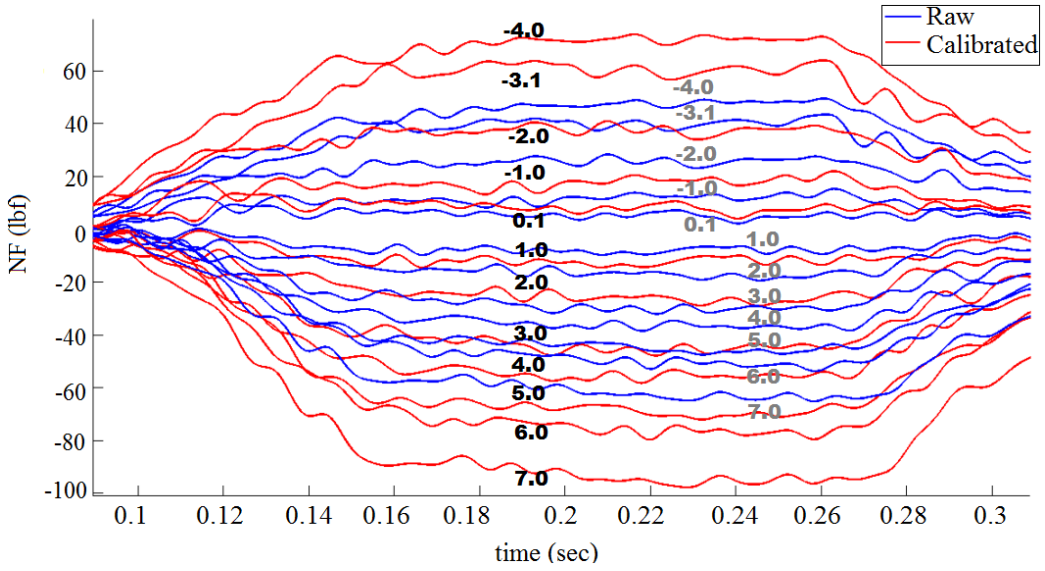

Figure 5.1. Change in *NF* component with change in α.

The closer values of the *NF* component at the lower α's create minimal adjustments to C_L, allowing the *CF* component to be the more dominant term in the calculation of the coefficients. This explains why C_D has a more significant change at the lower α's of less than 2°. However, as α increases to higher values over 5°, the dominant term in the drag becomes the *NF* component again, increasing C_D. The measured *NF*, *CF*, and *PM* components for a specified time frame are shown in Table 5.1 (see Fig. 2.13 for orientation).

Table 5.1. Numeric averages of the *NF*, *CF*, and *PM* components for each run of the parametric study in the time frame 0.18 – 0.25 s.

α	*NF*	*CF*	*PM*
$-4.0°$	71.759	–2.355	–1.377
$-3.1°$	60.608	–2.038	–1.949
$-2.0°$	37.648	–1.735	–3.749
$-1.0°$	17.627	–1.843	–2.211
$0.1°$	7.700	–2.200	2.2723
$1.0°$	–12.299	–2.109	4.479
$2.0°$	–26.097	–2.061	4.283
$3.0°$	–45.060	–2.097	5.792
$4.0°$	–55.640	–2.016	5.847
$5.0°$	–680861	–2.197	5.375
$6.0°$	–75.485	–1.486	8.564
$7.0°$	–94.082	–1.984	6.246

The numeric values and test conditions of the experimental data are shown in Table 5.2 for each run with the steady flow time chosen between 0.18 s and 0.25 s. The minimal variations in the test conditions can result in changes to the aerodynamic coefficient values, creating outliers within the data but not significantly enough to completely offset the data from the trend lines with 95% confidence. The test conditions for the study with variation were Mach 0.75 $\pm$ 0.015, Re = 3 million/inch $\pm$ 3000/inch, and $\alpha = -4°$ to $7°$ within $\pm$ $0.1°$.

The experimental results found follow the expected trend for the coefficients of lift and drag. A linear trend is seen in C_L, while C_D is a parabolic trend, as seen in Fig. 5.2. The variations in the results are due to the fluctuation in test conditions for each run because of the analog pressure gauge on the wind tunnel. The vertical error bars are found based on the propagation of error equation, explained in §5.4, while the horizontal error bars are based on the known error in α, which is $\pm$ $0.1°$.

Table 5.2. Numeric values and test conditions for each run of the parametric study using the time frame 0.18 – 0.25 s.

α	Mach No.	Re No.	C_L	C_D	C_M	L/D
$-4.0°$	0.764	3.06E6	–0.4564	0.0470	0.0044	–9.71
$-3.1°$	0.749	3.03E6	–0.3969	0.0349	0.0064	–11.38
$-2.0°$	0.754	3.13E6	–0.2384	0.0193	0.0119	–12.33
$-1.0°$	0.759	3.10E6	–0.1118	0.0137	0.0071	–8.16
$0.1°$	0.751	3.12E6	–0.0488	0.0139	–0.0088	–3.51
$1.0°$	0.751	3.15E6	0.0777	0.0146	–0.0141	5.30
$2.0°$	0.746	3.09E6	0.1679	0.0192	–0.0139	8.75
$3.0°$	0.751	3.10E6	0.2876	0.0285	–0.0185	10.08
$4.0°$	0.750	3.08E6	0.3564	0.0381	–0.0189	9.39
$5.0°$	0.754	3.04E6	0.4469	0.0535	–0.0175	8.36
$6.0°$	0.734	2.99E6	0.5073	0.0634	–0.0290	7.99
$7.0°$	0.743	3.01E6	0.6202	0.0895	–0.0208	6.93

From the experimental data, the drag polar can also be found, as seen in Fig. 5.3. The parabolic relationship of C_D to C_L is described by

$$C_D = C_{Do} + K_1 \cdot C_L + K_2 \cdot {C_L}^2 \tag{5.1}$$

where K_1 is usually zero for low values of C_{Lmin} in subsonic conditions [3]. In addition, C_{Do} is the parasitic drag coefficient, found when the lift is zero. With this information, the relationship between the experimental C_L and C_D was found to be

$$C_D(C_L) = 0.0121 + 0.01C_L + 0.1825{C_L}^2 \tag{5.2}$$

with an $R^2 = 0.997$. A large similarity between the subsonic theory and the results from the transonic data can be seen since the value of $K_1 = 0.01$, which is close to zero. By knowing the K coefficients and the minimum lift coefficient C_{Lmin}, the total drag coefficient C_D can be separated by the causing source.

The error bars for the drag polar and the C_L–C_D plot indicate that the data are within the 95% confidence interval found by the trendline shown. The larger

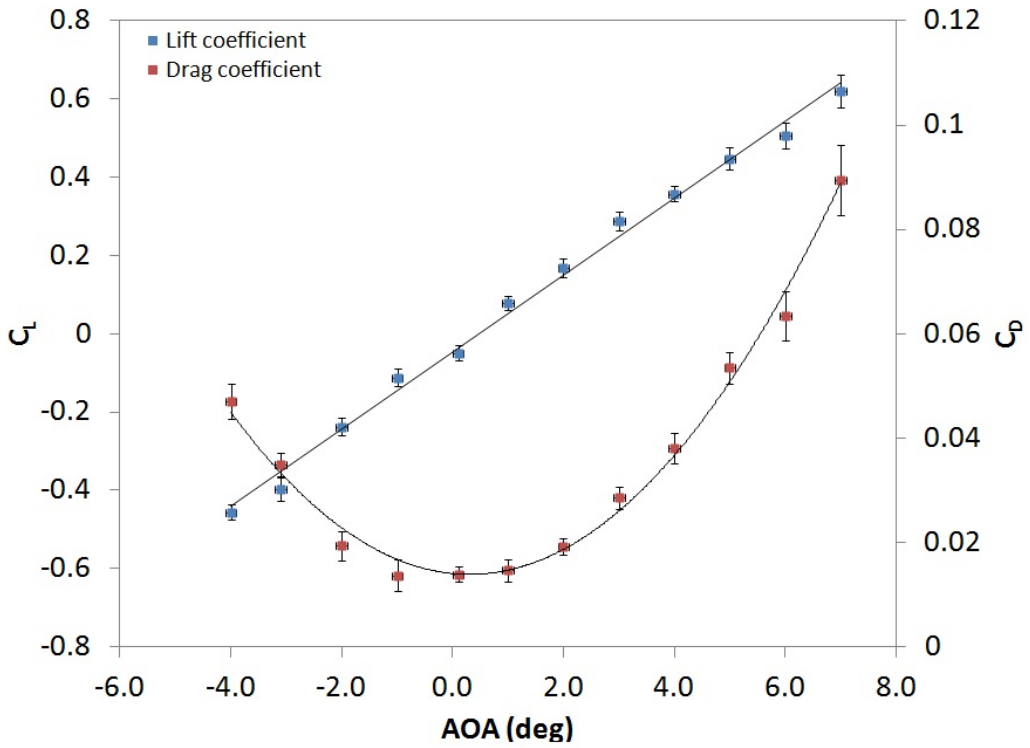

Figure 5.2. Parametric study of C_L and C_D for a NACA 0012 airfoil wingtip after dynamic calibration.

uncertainty bars at $\alpha = 6°$ and $7°$ for C_L and C_D signify that there is more variation in the results, due to a combination between the test conditions and the measurements. It is possible that some flow interaction is occurring on the airfoil surface, including shocks, buffeting, and wall interaction.

As seen in Fig. 5.4, C_M appears to have little variation as well, except for the aforementioned α's. The value of C_M is expected to have a value near zero and remains constant for each α. As can be seen, C_M remains relatively constant throughout for the positive and negative α's excluding $\alpha = 6°$ and $7°$. This departure at high α is possibly due to buffeting and shocks interacting with the airfoil, or the slightly different test conditions.

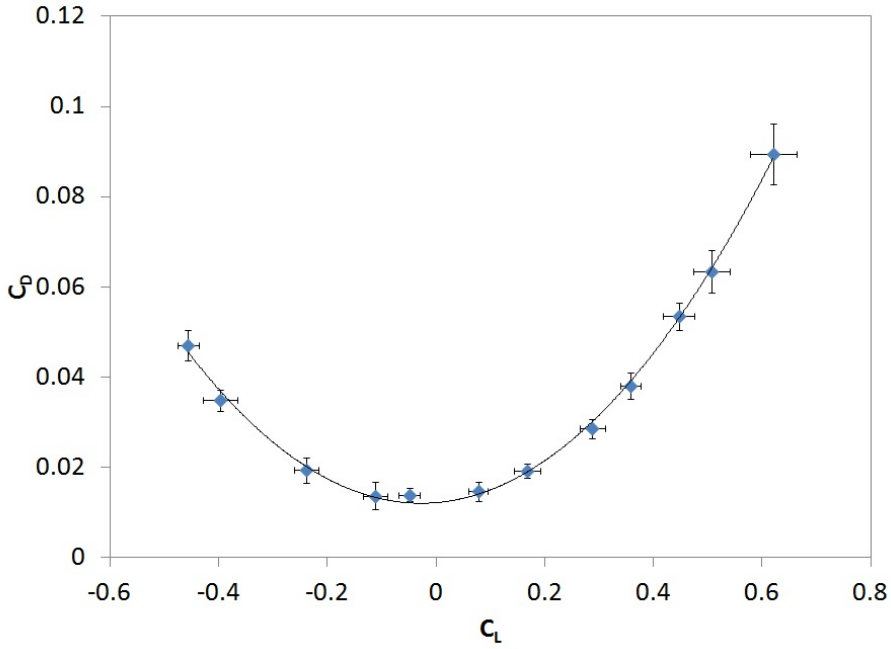

Figure 5.3. Parametric study of the drag polar for a NACA 0012 airfoil wingtip.

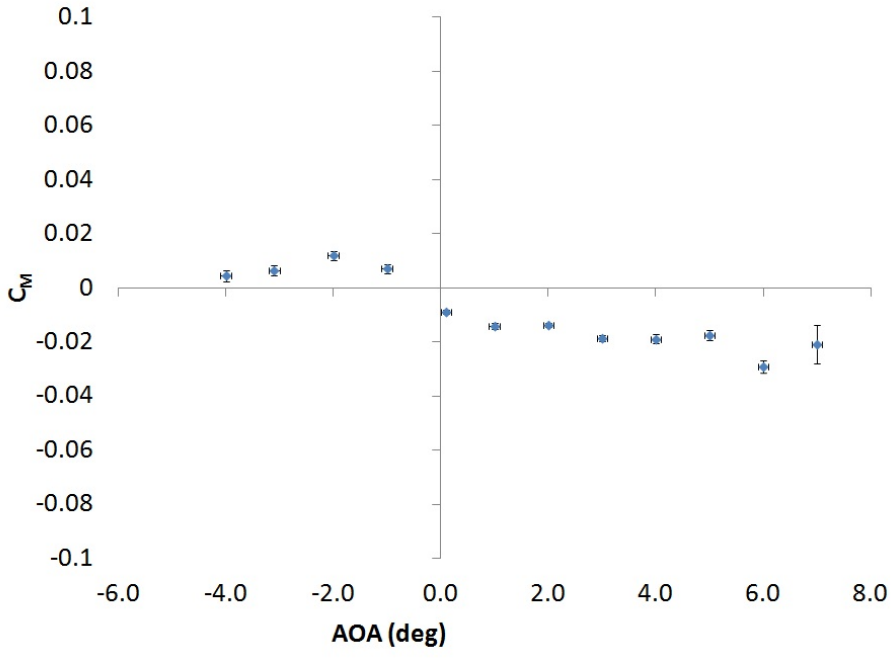

Figure 5.4. Parametric study of C_M for a NACA 0012 airfoil wingtip.

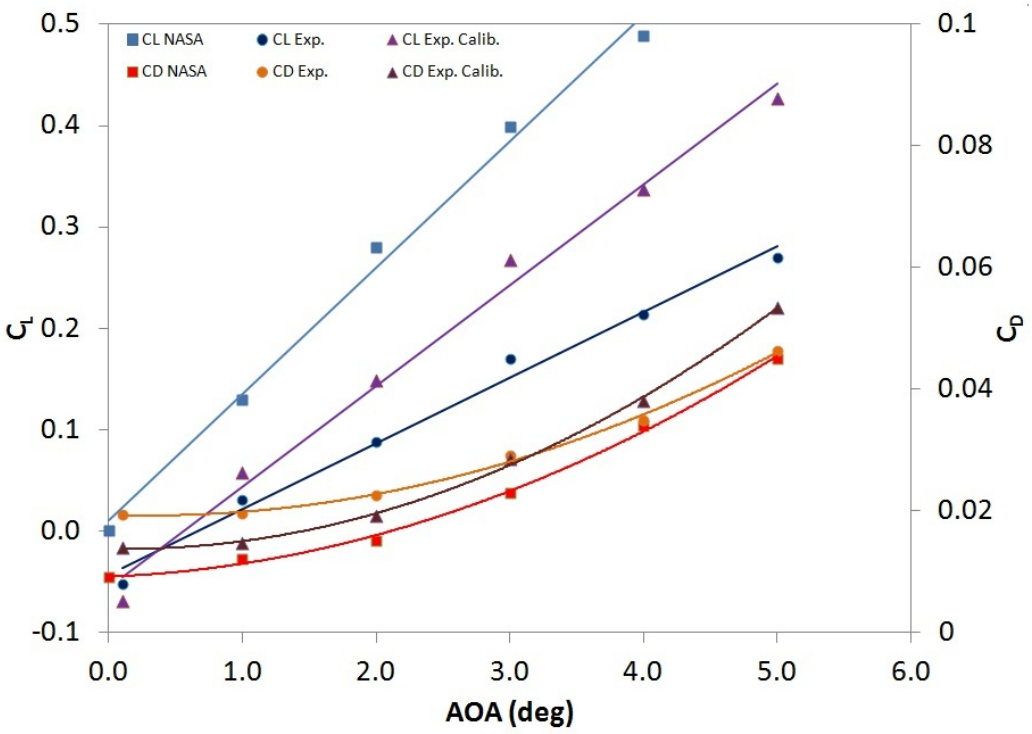

Figure 5.5. Comparison of the lift and drag coefficients of the published data [6], uncalibrated data, and calibrated data.

The comparison of the experimental data, both calibrated and uncalibrated, to the published data of [6] for C_L and C_D is presented in Fig. 5.5. As expected the values are not exact when comparing two-dimensional data with the experimental three-dimensional data. However, the trend for C_D of the calibrated experimental data is the same as that for the published data but shifted up on the ordinate of the plot. This is due to the increment caused by the induced drag found in finite wings. The uncalibrated data for C_D do not resemble the published data with its trend, crossing both curves of the drag coefficient.

The trend for C_L of the published data has a much higher slope due to the infinite wing characteristics, resulting in higher values of C_L than the experimental data. The finite wing produces a lower lift slope curve because of the downwash

reducing the effective angle of attack, but is considerably closer than the uncalibrated data. The uncalibrated C_L has an even lower slope value since vibrations have not been excluded.

5.4 Uncertainty Analysis

The uncertainty in each of the measured quantities was calculated using the 95% confidence interval, defined in Eqn. (5.3) [27]. The $\bar{x}$ represents the calculated average of the number of points N and x_i is the exact value of point i from 1 to N, where x is the measured quantity of interest. This was used for the Mach and Reynolds numbers, the dynamic pressure, and the measured forces and moments:

$$u_{95\%} = \pm 2\sqrt{\frac{\sum \left(\bar{x} - x_i\right)^2}{N}} \tag{5.3}$$

Using these calculated uncertainties for the measured quantities, the uncertainty of the aerodynamic coefficients can be found using the propagation of error equation [27]. Shown in Eqn. (5.4) is the calculation for uncertainty in C_L using the averaged values within the partial derivative of the equation for C_L (see §2.4). The uncertainty $u_\alpha = \pm 0.1^\circ$ based on the digital angle finder tool used. As seen in Eqns. (5.5) and (5.6), the uncertainty for C_D has the same four terms while C_M has the PM component and the dynamic pressure q.

$$u_{C_L} = \pm\sqrt{\left(\frac{\partial C_L}{\partial NF}u_{NF}\right)^2 + \left(\frac{\partial C_L}{\partial CF}u_{CF}\right)^2 + \left(\frac{\partial C_L}{\partial q}u_q\right)^2 + \left(\frac{\partial C_L}{\partial \alpha}u_\alpha\right)^2} \tag{5.4}$$

$$u_{C_D} = \pm\sqrt{\left(\frac{\partial C_D}{\partial NF}u_{NF}\right)^2 + \left(\frac{\partial C_D}{\partial CF}u_{CF}\right)^2 + \left(\frac{\partial C_D}{\partial q}u_q\right)^2 + \left(\frac{\partial C_D}{\partial \alpha}u_\alpha\right)^2} \tag{5.5}$$

$$u_{C_M} = \pm\sqrt{\left(\frac{\partial C_M}{\partial PM} u_{PM}\right)^2 + \left(\frac{\partial C_M}{\partial q} u_q\right)^2} \tag{5.6}$$

These calculated uncertainties are shown as vertical error bars in Figs. 5.2 and 5.4, with the values shown in Table 5.3. The uncertainties remain low, except for the higher α's. The test conditions can be mostly blamed since the exact same pressure was most likely not reached as with the other cases, reducing the forces on the airfoil. Other interactions on the airfoil at the high α's include buffeting, side wall interference, and shocks on the surface.

Table 5.3. Calculated uncertainties of the aerodynamic coefficients for each run in the parametric study for the time frame 0.18 – 0.25 s.

α	u_{C_L}	u_{C_D}	u_{C_M}
$-4.0°$	0.0197	0.00343	0.00218
$-3.1°$	0.0313	0.00233	0.00181
$-2.0°$	0.0227	0.00279	0.00173
$-1.0°$	0.0226	0.00295	0.00176
$0.1°$	0.0197	0.00154	0.00073
$1.0°$	0.0177	0.00219	0.00116
$2.0°$	0.0237	0.00163	0.00079
$3.0°$	0.0235	0.00222	0.00119
$4.0°$	0.0191	0.00298	0.00172
$5.0°$	0.0285	0.00307	0.00180
$6.0°$	0.0332	0.00480	0.00225
$7.0°$	0.0432	0.00679	0.00709

CHAPTER 6

CONCLUSIONS AND FUTURE WORK

6.1 Summary of Work and Results

The calibration of the force balance with the NACA 0012 wingtip produces aerodynamic force data within a 95% confidence interval. The force balance is now supporting equipment that is capable of data acquisition for basic research and validation tests at high Reynolds numbers within the transonic regime. The static calibration performed provides results of the *NF*, *CF*, and *PM* components within 0.5% accuracy for loads up to their maximum value, while the *MX* and *MZ* components have results within 10%. However, the sudden loading applied to the model during experiments produces some error in the measurements. The dynamic calibration increases the accuracy of applied aerodynamic loads by removing unwanted signals within the measurements, including vibrations and signal interference. The parametric study performed validates the calibration process with the comparison to the data from Mineck and Hartwich [6], knowing that the differences in the data are expected for comparing two-dimensional with three-dimensional data. Since data are limited for this airfoil in the transonic regime and transonic effects of the Reynold's number affects force data, the comparison of [6] to the experimental data found is most useful at this time. By calibrating the force balance and confirming the results found at the chosen conditions, further testing can be done to calculate the aerodynamic effects of transonic speeds on a NACA 0012 wingtip. The dynamic calibration performed specifically applies to the mounted model[1] on the force balance.

[1]NACA 0012 wingtip.

6.1.1 Matlab Program for Analyzing Data

The code developed for analyzing the force measurements and the test conditions can be found in App. C. The angle of attack, steady flow time frame, and unit selection are required inputs after running the program, while the sample rate, offset of the thermocouple, and file location are edited before running the program. The planform area is set for the current model, a NACA 0012 wingtip. The vectors created from the input Excel file are based on the current output by the LabVIEW program.

The unit selection was added to the code for versatility in order to provide both metric and English unit systems to the user. However, the error analysis is only valid when the English unit system is chosen due to the complexity of the uncertainty calculations. The offset of the thermocouple is set at zero for a sample rate of 50 kHz or less, but would need to be changed if a higher sample rate is required.

After correcting the measurements with the vector-matrix dot product iterations, a low-pass filter is applied to remove some of the noise within the signal. However, the application of the transfer function is done to the raw, non-filtered data where the transfer functions are taken from custom function files in Matlab created from the dynamic calibration analysis. The first five figures generated by the program are the force and moment measurements for the test time, where the NF and CF components' plots show the change in readings with and without the dynamic calibration. The unit system chosen is also shown on the ordinate of the plots.

The pressure and temperature data are also analyzed within the program, calculating the test conditions during the sampling time of the data to provide the Mach and Reynolds numbers, as well as the dynamic pressure, within the steady flow test time. The next three figures show the test conditions and the steady flow time frame with the option to plot the temperature in another.

The numeric values are then vectorized and averaged based on the stead flow time frame chosen for the force measurements and the test conditions. The aerodynamic coefficients are then calculated using Eqns. (2.10) based on the averages of the measurements. The variation of the coefficients in time can also be plotted if necessary. Lastly, the errors of the measured quantities and the uncertainty in the calculated coefficients are found from Eqns. (5.3) through (5.6) in §5.4.

6.1.2 Transonic Tunnel Operator's Manual

The operator's manual for the transonic facility at the Aerodynamics Research Center at UTA was outdated, so new information was added for running the tunnel, acquiring data, and maintaining the facility. This includes the current procedures for conducting an experiment, the current equipment and instrumentation in use for data acquisition, and the theory behind the operation of the tunnel and how to alter the test conditions. References about the facility, its history, and previous theses and dissertations utilizing the facility were also included. More pictures of supporting equipment and plots of test capabilities were also added to provide increased detail about the tunnel.

6.1.3 Surface Flow Visualization

Although surface flow visualization (SFV) was not a fully investigated topic towards the research, the application can be applied with the force measurements. The SFV with fluorescent paint provides information about the flow over the top surface of the model, showing the transition point, shock position, and flow separation, as seen in Fig. 6.1. In correlation with the force measurements, the position of the shock on the surface of the airfoil can be used in conjunction with the test conditions

and the aerodynamic coefficients to determine how the position of the shock affects the lift and drag.

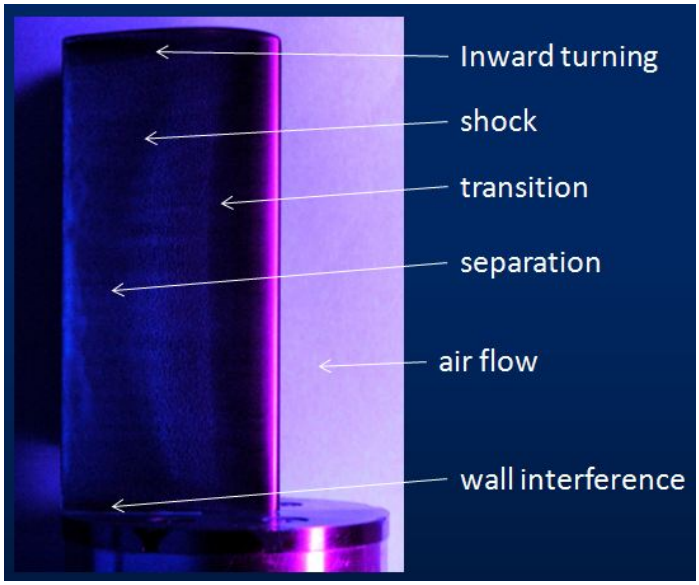

Figure 6.1. An example of surface flow visualization with labels of the assumed surface flow effects.

6.2 Future Work

A large array of research and validation tests can now be conducted with the force balance and NACA 0012 wingtip properly calibrated. This includes, but is not limited to, Mach number sweeps, Reynolds number sweeps, and angle of attack sweeps, which can be verified with previous data as well as computational fluid dynamics (CFD) analysis. In addition, the SFV can be investigated and analyzed concurrently with these sweeps and related to the force measurements found.

Since solid walls are required on the sides of the test section when using the force balance, wall interference should also be investigated to determine the effects on the measurements and how it can be compensated.

If force measurements are required for other airfoil models, the dynamic calibration process needs to be repeated. The procedures outlined in Chap. 4 should be followed to obtain true aerodynamic forces.

APPENDIX A

STATIC CALIBRATION DATA

A.1 Sensitivity Constants

Graphs of sensitivity constants.

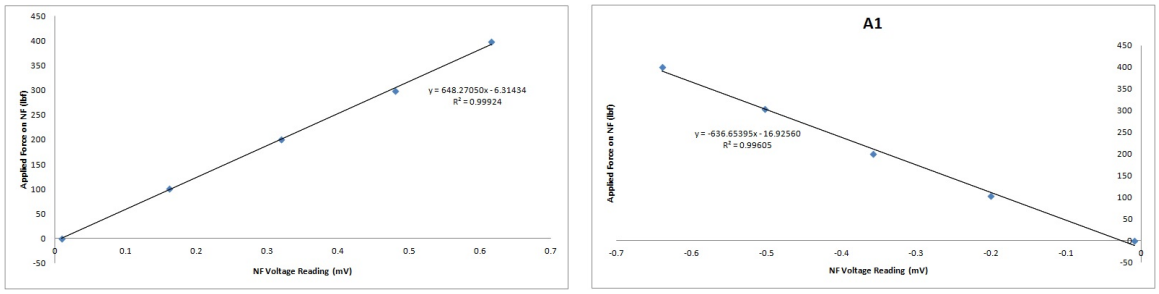

Figure A.1. Sensitivity constant of NF component from A and A1.

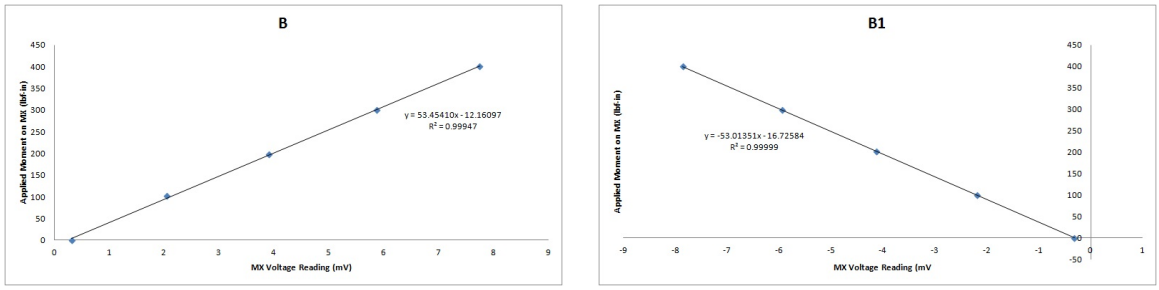

Figure A.2. Sensitivity constant of MX component from B and B1.

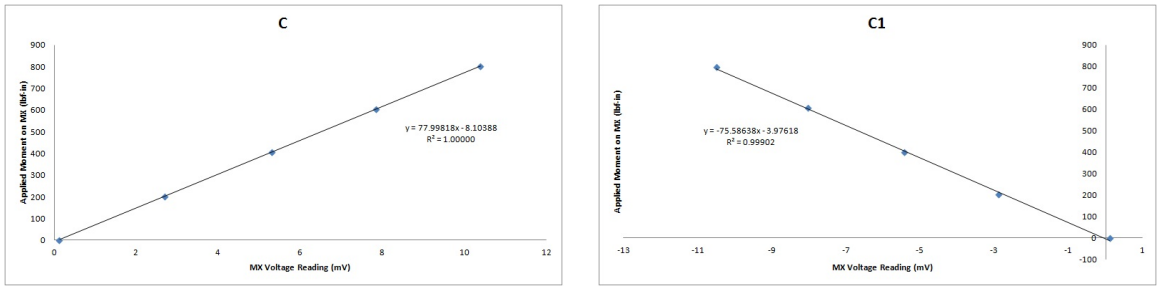

Figure A.3. Sensitivity constant of MX component from C and C1.

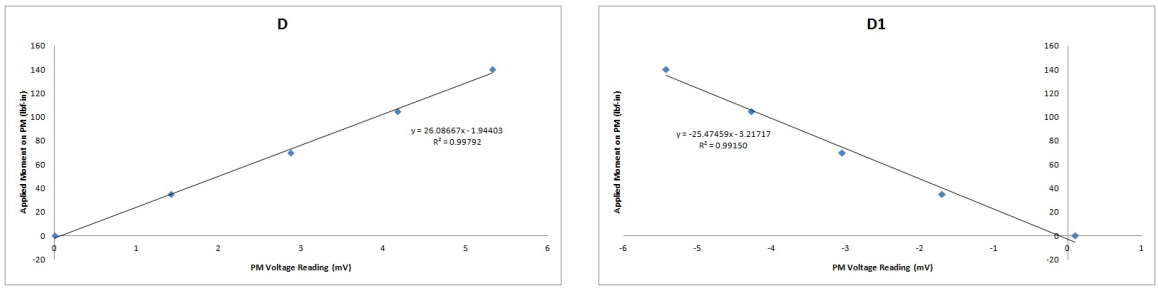

Figure A.4. Sensitivity constant of PM component from D and D1.

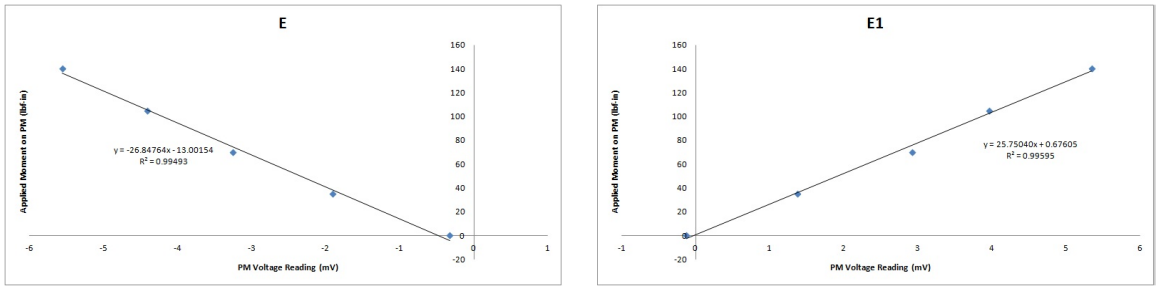

Figure A.5. Sensitivity constant of PM component from E and E1.

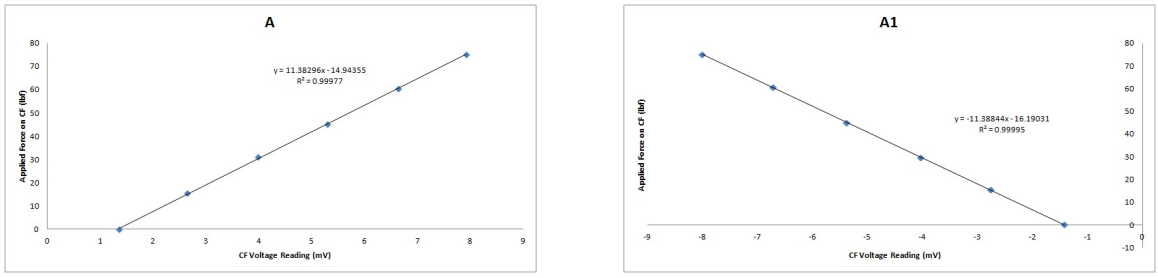

Figure A.6. Sensitivity constant of CF component from A and A1.

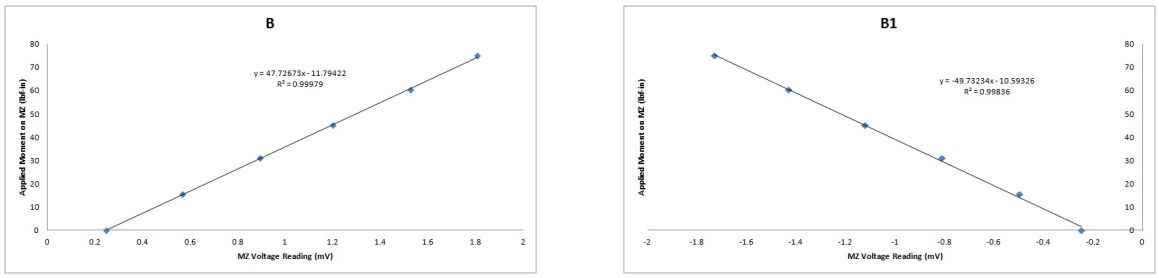

Figure A.7. Sensitivity constant of MZ component from B and B1.

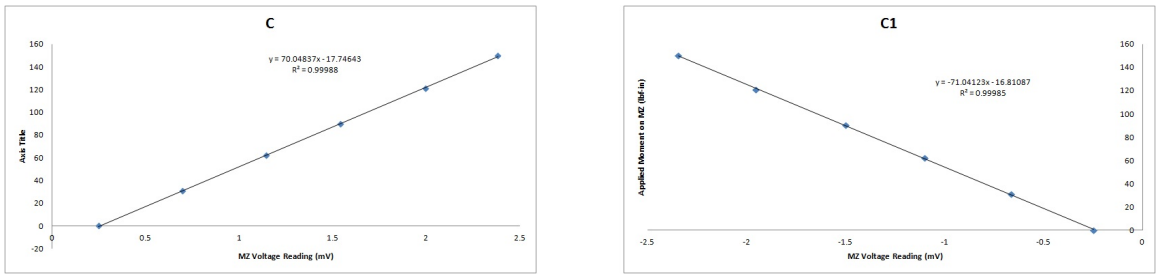

Figure A.8. Sensitivity constant of MZ component from C and C1.

Table A.1. Current and previous sensitivity constants of the components of the force balance.

Component	**Current S Constant**	**Previous S Constant**	
NF	642.462225	630.51702	(lbf/mV)
MX	131.941535	147.95088	(lbf-in/mV)
CF	11.38500	11.79616	(lbf/mV)
MZ	119.27487	137.74105	(lbf-in/mV)
PM	26.039825	24.88447	(lbf-in/mV)

.

A.2 Interaction Coefficients

The interaction equations for the NF plane are

$$NF = \frac{A - A1}{2} \tag{A.1a}$$

$$NF^2 = \frac{A + A1}{2} \tag{A.1b}$$

$$MX = (C - C1) - (B - B1) \tag{A.1c}$$

$$MX^2 = (C + C1) - 2\,(B + B1) + (A + A1) \tag{A.1d}$$

$$NF \times MX = 2\,(B + B1) - 0.5\,(C + C1) - 1.5\,(A + A1) \tag{A.1e}$$

$$PM = \frac{(D - D1) - (E - E1)}{4} \tag{A.1f}$$

$$PM^2 = \frac{(D + D1) + (E + E1)}{4} \tag{A.1g}$$

$$NF \times PM = 6.25\,[(D - E) + (D1 - E1)] \tag{A.1h}$$

while those based on the CF plane are

$$CF = \frac{A - A1}{2} \tag{A.2a}$$

$$CF^2 = \frac{A + A1}{2} \tag{A.2b}$$

$$MZ = (C - C1) - (B - B1) \tag{A.2c}$$

$$MZ^2 = (C + C1) - 2\,(B + B1) + (A + A1) \tag{A.2d}$$

$$CF \times MZ = 2\,(B + B1) - 0.5\,(C + C1) - 1.5\,(A + A1) \tag{A.2e}$$

		LOAD AMT				
	Load Pt	NF	MX	CF	MZ	PM
+NF PLANE	A	398.0	0.0	0.0	0.0	0.0
	B	400.5	400.5	0.0	0.0	0.0
	C	401.0	802.0	0.0	0.0	0.0
	D	20.0	0.0	0.0	0.0	140.0
	E	20.0	0.0	0.0	0.0	-140.0
-NF PLANE	A1	-399.5	0.0	0.0	0.0	0.0
	B1	-400.5	-400.5	0.0	0.0	0.0
	C1	-398.0	-796.0	0.0	0.0	0.0
	D1	-20.0	0.0	0.0	0.0	-140.0
	E1	-20.0	0.0	0.0	0.0	140.0
+CF PLANE	A	0.0	0.0	75.0	0.0	0.0
	B	0.0	0.0	75.0	75.0	0.0
	C	0.0	0.0	75.0	150.0	0.0
-CF PLANE	A1	0.0	0.0	-75.0	0.0	0.0
	B1	0.0	0.0	-75.0	-75.0	0.0
	C1	0.0	0.0	-75.0	-150.0	0.0

Figure A.9. Values of the maximum loads used for each load point (lbf & lbf·in.).

The interaction vector is set up in the following order

$$X = \begin{bmatrix} NF \\ NF^2 \\ MX \\ MX^2 \\ NF \times MX \\ PM \\ PM^2 \\ NF \times PM \\ CF \\ CF^2 \\ MZ \\ MZ^2 \\ CF \times MZ \end{bmatrix} \tag{A.3}$$

	Load Pt	NF	MX	CF	MZ	PM
Sensitivity Constant		642.46223	131.94154	11.385	119.27487	26.039825
+NF PLANE	A	0.606615	4.817348	-0.064993	-0.050290	-0.424923
	B	0.526589	7.432047	-0.025603	0.055875	-0.929080
	C	0.479512	10.075123	-0.003296	-0.043712	-0.777561
	D	0.011838	0.268519	0.045986	-0.035583	5.323025
	E	0.054613	0.228266	-0.057736	0.012292	-5.557416
-NF PLANE	A1	-0.630346	-4.995186	0.027586	0.108115	-0.045612
	B1	-0.556599	-7.547360	0.004913	0.073637	-0.138433
	C1	-0.493569	-10.187297	0.028502	0.135560	-0.275879
	D1	0.001068	-0.234197	-0.027954	0.029234	-5.431421
	E1	-0.042293	-0.224252	0.053678	0.005341	5.345056
+CF PLANE	A	-0.021647	-0.040624	6.555340	1.061888	-0.313903
	B	-0.023392	-0.041215	6.587894	1.559276	-0.038191
	C	-0.019880	-0.039533	6.680807	2.134019	-0.117797
-CF PLANE	A1	0.033598	0.121490	-6.585339	-0.995511	-0.473160
	B1	-0.016722	-0.141721	-6.588662	-1.483834	-0.319048
	C1	-0.013914	-0.135252	-6.774390	-2.098067	-0.408288

Figure A.10. Component readings (mV) corresponding to the applied loads.

A.3 Balance Matrix

Table A.2. The almighty balance matrix.

	NF	MX	CF	MZ	PM
NF	0.00000E+00	1.62914E+00	–1.32630E–03	–2.37747E–02	–1.24288E–02
NF^2	–4.82826E–05	–7.43067E–05	–1.34866E–06	2.18416E–05	–3.88019E–05
MX	–1.01484E–01	0.00000E+00	–2.09299E–05	–2.76365E–02	1.07950E–02
MX^2	2.93950E–05	–1.61264E–05	6.83769E–07	–2.68440E–05	3.27483E–05
$NF{\times}MX$	–4.03456E–05	4.39295E–05	8.73557E–08	5.44168E–05	–8.48497E–05
PM	–9.81294E–02	1.17446E–02	3.74196E–03	–1.51792E–02	0.00000E+00
PM^2	2.03841E–04	6.36181E–05	2.00105E–06	1.69296E–05	–1.05052E–04
$NF{\times}PM$	4.19863E–05	4.46147E–04	2.80591E–05	–3.19131E–04	3.02033E–04
CF	–2.37241E–01	–1.42972E–01	0.00000E+00	1.64027E+00	2.77195E–02
CF^2	6.86131E–04	9.53400E–04	–3.05192E–05	7.07454E–04	–1.83137E–03
MZ	3.19279E–03	–4.45446E–03	2.23695E–02	0.00000E+00	1.76904E–03
MZ^2	1.86516E–03	1.78415E–03	–6.90900E–05	–2.87964E–04	–7.75144E–04
$CF{\times}MZ$	–4.92126E–03	–4.97230E–03	9.68641E–05	3.74891E–04	1.78986E–03

.

A.4 Finding the Forces

A detailed version of Eqn. 3.2 can be seen below. **M** can be seen in the previous section, A.3.

$$\begin{bmatrix} NF^{[i+1]} \\ MX^{[i+1]} \\ CF^{[i+1]} \\ MZ^{[i+1]} \\ PM^{[i+1]} \end{bmatrix} = \begin{bmatrix} NF^{[0]} \\ MX^{[0]} \\ CF^{[0]} \\ MZ^{[0]} \\ PM^{[0]} \end{bmatrix} - M \cdot \begin{bmatrix} NF^{[i]} \\ [NF^2]^{[i]} \\ MX^{[i]} \\ MX^{2[i]} \\ [NF \times MX]^{[i]} \\ PM^{[i]} \\ [PM^2]^{[i]} \\ [NF \times PM]^{[i]} \\ CF^{[i]} \\ [CF^2]^{[i]} \\ MZ^{[i]} \\ [MZ^2]^{[i]} \\ [CF \times MZ]^{[i]} \end{bmatrix} \tag{A.4}$$

where

- 0 = uncorrected measurement
- i = iteration number
- **M** = balance matrix in App. A.3

.

A.5 Static Load Accuracy Check

A	NF	MX	CF	MZ	PM
Reading	0.607	4.817	-0.065	-0.050	-0.425
App. Load	*398.0*	*0.0*	*0.0*	*0.0*	*0.0*
Uncorr. Load	389.7271	635.608349	-0.7399425	-4.2244778	-11.02922
Avg from Matlab	*397.3024*	*0.0762*	*8.04E-04*	*0.0198*	*-0.0151*
Difference	0.69760	-0.07620	-0.00080	-0.01980	-0.01510
%Error (Full Load)	**0.1395%**	**0.0076%**	**0.0011%**	**0.0132%**	**0.0108%**

A1	NF	MX	CF	MZ	PM
Reading	-0.630	-4.995	0.028	0.108	-0.046
App. Load	*-399.5*	*0.0*	*0.0*	*0.0*	*0.0*
Uncorr. Load	-404.97353	-659.0725	0.3140709	9.0818567	-1.1839057
Avg from Matlab	*-396.6873*	*-0.1009*	*0.3028*	*-7.483*	*7.5975*
Applied - Matlab	2.81270	-0.10090	-0.30280	-7.48300	-7.59750
%Error (Full Load)	**0.5625%**	**0.0101%**	**0.4037%**	**4.9887%**	**5.4268%**

B	NF	MX	CF	MZ	PM
Reading	0.527	7.432	-0.026	0.056	-0.929
App. Load	*400.5*	*400.5*	*0.0*	*0.0*	*0.0*
Uncorr. Load	338.31362	980.595718	-0.2914941	4.6936048	-24.115051
Avg from Matlab	*401.0447*	*362.7356*	*0.4859*	*6.9346*	*-2.6563*
Applied - Matlab	-0.54470	37.76440	-0.48590	-6.93460	-2.65630
Error	**0.1089%**	**3.7764%**	**0.6479%**	**4.6231%**	**1.8974%**

B1	NF	MX	CF	MZ	PM
Reading	-0.557	-7.547	0.005	0.074	-0.138
App. Load	*-400.5*	*-400.5*	*0.0*	*0.0*	*0.0*
Uncorr. Load	-357.59351	-995.81031	0.0559314	6.1856544	-3.5931362
Avg from Matlab	*-400.5582*	*-361.9074*	*-0.1007*	*-14.2195*	*11.2512*
Applied - Matlab	-0.05820	38.59260	-0.10070	-14.21950	-11.25120
%Error (Full Load)	**0.0116%**	**3.8593%**	**0.1343%**	**9.4797%**	**8.0366%**

C	NF	MX	CF	MZ	PM
Reading	0.480	10.075	-0.003	-0.044	-0.778
App. Load	*401.5*	*803.0*	*0.0*	*0.0*	*0.0*
Uncorr. Load	308.06851	1329.32717	-0.0375204	-3.671877	-20.182239
Avg from Matlab	*400.7774*	*711.8325*	*0.4771*	*7.0956*	*-2.8975*
Applied - Matlab	0.72260	91.16750	-0.47710	-7.09560	-2.89750
%Error (Full Load)	**0.1445%**	**9.1168%**	**0.6361%**	**4.7304%**	**2.0696%**

C1	NF	MX	CF	MZ	PM
Reading	-0.494	-10.187	0.029	0.136	-0.276
App. Load	*-398.0*	*-796.0*	*0.0*	*0.0*	*0.0*
Uncorr. Load	-317.09952	-1344.1276	0.3244942	11.387275	-7.1606646
Avg from Matlab	*-400.743*	*-710.0298*	*-0.1142*	*-14.0556*	*11.0073*
Applied - Matlab	-2.74300	85.97020	-0.11420	-14.05560	-11.00730
%Error (Full Load)	**0.5486%**	**8.5970%**	**0.1523%**	**9.3704%**	**7.8624%**

D	NF	MX	CF	MZ	PM
Reading	-0.025	0.087	0.039	0.033	5.112
App. Load	*20.0*	*0.0*	*0.0*	*0.0*	*140.0*
Uncorr. Load	-15.882864	11.4557373	0.4402781	2.8139663	132.67932
Avg from Matlab	*17.5056*	*2.9241*	*-0.0601*	*-0.7419*	*140.1231*
Applied - Matlab	2.49440	-2.92410	-0.06010	-0.74190	-0.12310
%Error (Full Load)	**0.4989%**	**0.2924%**	**0.0801%**	**0.4946%**	**0.0879%**

D1	NF	MX	CF	MZ	PM
Reading	-0.001	-0.281	-0.044	0.014	-5.594
App. Load	*-20.0*	*0.0*	*0.0*	*0.0*	*-140.0*
Uncorr. Load	-0.4365675	-37.056284	-0.5051609	1.2062735	-145.20742
Avg from Matlab	*-17.5376*	*-3.0126*	*0.0477*	*0.8845*	*-140.3042*
Applied - Matlab	**2.46240**	**-3.01260**	**-0.04770**	**-0.88450**	**-0.30420**
%Error (Full Load)	**0.4925%**	**0.3013%**	**0.0636%**	**0.5897%**	**0.2173%**

E	NF	MX	CF	MZ	PM
Reading	0.0546133	0.22826556	-0.0577356	0.0122925	-5.5574162
App. Load	*20.0*	*0.0*	*0.0*	*0.0*	*-140.0*
Uncorr. Load	35.086957	30.1177088	-0.6573201	1.0325905	-144.24738
Avg from Matlab	*17.4778*	*3.1259*	*-0.0456*	*-0.8587*	*-141.6662*
Applied - Matlab	2.52220	-3.125900	-0.045600	-0.858700	-1.66620
%Error (Full Load)	**0.5044%**	**0.3126%**	**0.0608%**	**0.5725%**	**1.1901%**

E1	NF	MX	CF	MZ	PM
Reading	-0.042293	-0.2242517	0.0536775	0.0053412	5.3450562
App. Load	*-20.0*	*0.0*	*0.0*	*0.0*	*140.0*
Uncorr. Load	-27.171667	-29.58812	0.6111184	0.4486696	138.7354
Avg from Matlab	*-17.5777*	*-2.7538*	*0.0642*	*0.7581*	*141.8552*
Applied - Matlab	2.42230	-2.75380	-0.06420	-0.75810	-1.85520
%Error (Full Load)	**0.4845%**	**0.2754%**	**0.0856%**	**0.5054%**	**1.3251%**

Figure A.11. Accuracy check for the load points on the positive and negative NF plane.

A	NF	MX	CF	MZ	PM
Reading	-0.022	-0.041	6.555	1.062	-0.314
App. Load	*0.0*	*0.0*	*75.0*	*0.0*	*0.0*
Uncorr. Load	-13.90712	-5.360031	74.632546	89.200652	-8.147612
Avg from Matlab	*2.1449*	*-3.6738*	*75.068*	*-0.4161*	*-0.2378*
Applied - Matlab	-2.14490	-3.67380	-0.06800	-0.41610	-0.23780
%Error (Full Load)	**0.4290%**	**0.3674%**	**0.0907%**	**0.2774%**	**0.1699%**

A1	NF	MX	CF	MZ	PM
Reading	0.034	0.121	-6.585	-0.996	-0.473
App. Load	*0.0*	*0.0*	*-75.0*	*0.0*	*0.0*
Uncorr. Load	21.58566	16.0296	-74.97409	-83.62482	-12.28126
Avg from Matlab	*0.4047*	*-0.2101*	*-75.228*	*0.2868*	*0.0947*
Applied - Matlab	-0.4047	-0.2101	-0.2280	-0.2868	-0.0947
%Error (Full Load)	**0.0809%**	**0.0210%**	**0.3040%**	**0.1912%**	**0.0676%**

B	NF	MX	CF	MZ	PM
Reading	-0.023	-0.041	6.588	1.559	-0.038
App. Load	*0.0*	*0.0*	*75.0*	*75.0*	*0.0*
Uncorr. Load	-15.02874	-5.437928	75.003177	130.98221	-0.991267
Avg from Matlab	*9.8886*	*0.3496*	*71.9115*	*62.407*	*1.8225*
Applied - Matlab	-9.88860	-0.34960	3.08850	12.59300	-1.82250
%Error (Full Load)	**1.9777%**	**0.0350%**	**4.1180%**	**8.3953%**	**1.3018%**

B1	NF	MX	CF	MZ	PM
Reading	-0.017	-0.142	-6.589	-1.484	-0.319
App. Load	*0.0*	*0.0*	*-75.0*	*-75.0*	*0.0*
Uncorr. Load	-10.74301	-18.69889	-75.01192	-124.6449	-8.281148
Avg from Matlab	*6.7035*	*-0.8793*	*-71.9619*	*-61.264*	*3.9702*
Applied - Matlab	-6.70350	-0.87930	3.03810	13.73600	-3.97020
%Error (Full Load)	**1.3407%**	**0.0879%**	**4.0508%**	**9.1573%**	**2.8359%**

C	NF	MX	CF	MZ	PM
Reading	-0.020	-0.040	6.681	2.134	-0.118
App. Load	*0.0*	*0.0*	*75.0*	*150.0*	*0.0*
Uncorr. Load	-12.77197	-5.216051	76.060993	179.26175	-3.057509
Avg from Matlab	*12.6329*	*-2.4926*	*72.4928*	*131.3931*	*0.8302*
Applied - Matlab	-12.6329	-2.49260	2.50720	18.60690	-0.83020
%Error (Full Load)	**2.5266%**	**0.2493%**	**3.3429%**	**12.4046%**	**0.5930%**

C1	NF	MX	CF	MZ	PM
Reading	-0.014	-0.135	-6.774	-2.098	-0.408
App. Load	*0.0*	*0.0*	*-75.0*	*-150.0*	*0.0*
Uncorr. Load	-8.939027	-17.8453	-77.12643	-176.2417	-10.59746
Avg from Matlab	*7.8626*	*-5.3353*	*-72.2788*	*-139.257*	*4.027*
Applied - Matlab	-7.86260	-5.33530	2.72120	10.74300	-4.02700
%Error (Full Load)	**1.5725%**	**0.5335%**	**3.6283%**	**7.1620%**	**2.8764%**

Figure A.12. Accuracy check for the load points on the positive and negative CF plane.

APPENDIX B

DYNAMIC CALIBRATION DATA

B.1 Matlab Code for the Dynamic Calibration of *CF*

```
TestData = ['FileName']; SheetName = ['Transonic']; SampleRate = 50000;
Time = xlsread(TestData,SheetName,'a24:a50023');
Input = xlsread(TestData,SheetName,'c24:c50023');
Input=-1*Input;
Output1 = xlsread(TestData,SheetName,'l24:l50023');
Input2 = xlsread('FileName2','Transonic','c24:c50023');
Input2=-1*Input2;
Output2 = xlsread('FileName2','Transonic','l24:l50023');
Force =Input;
U1=fft(Force);
Force2=Input2;
U2=fft(Force2);
Y1=fft(Output1*10^3);
G1=Y1./U1;
Y2=fft(Output2*10^3);
O2 = G1.*U2;
O2prime = ifft(O2);
figure(1)
plot(Time,O2prime,'b','linewidth',2)
hold on
plot(Time,Output2*10^3,'r')
hold on
legend('FFT','Actual','Filtered Actual','Filtered FFT')
xlabel('time (sec)'); ylabel('Output (mV)')
```

.

B.2 Dynamic Responses at Different Sampling Rates for *CF*

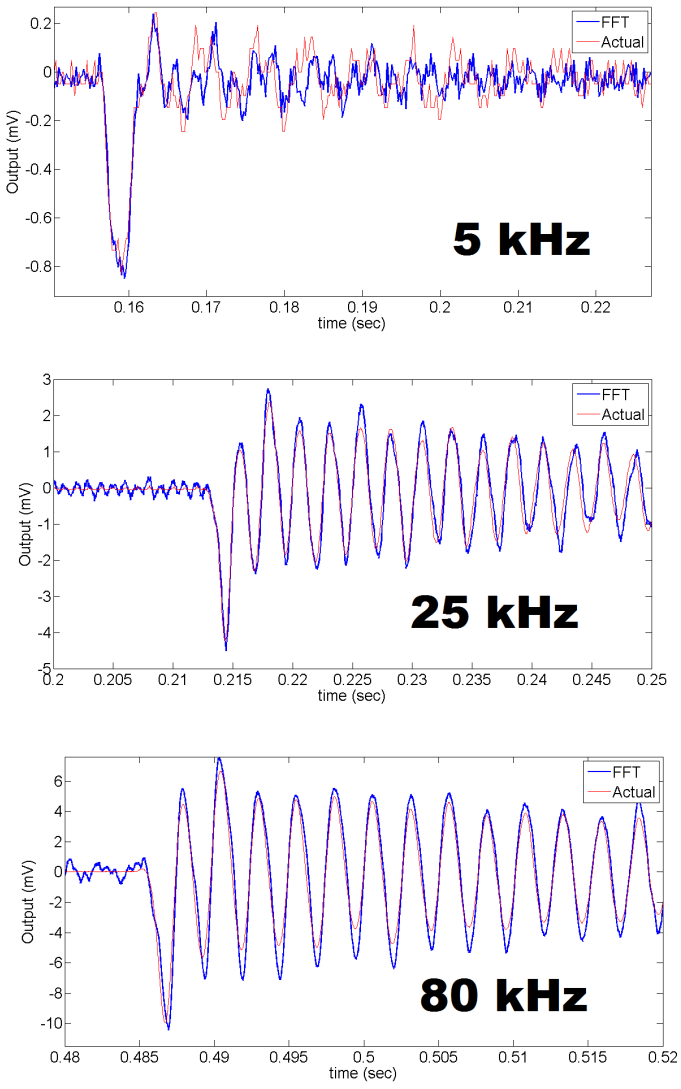

Figure B.1. Transformed data versus actual data for the *CF* component at 5 kHz, 25 kHz, and 80 kHz.

.

B.3 Matlab Code for the Dynamic Calibration of *NF*

```
TestData = ['FileName1']; SheetName = ['Transonic']; SampleRate = 50000;
Time = xlsread(TestData,SheetName,'a24:a50023');
Input = xlsread(TestData,SheetName,'c24:c50023');
Input=1*Input;
Output1a = xlsread(TestData,SheetName,'j24:j50023');
Output1b = xlsread(TestData,SheetName,'k24:k50023');
out1=Output1b-Output1a;
Input2 = xlsread('FileName2','Transonic','c24:c50023');
Input2=1*Input2;
Output2a = xlsread('FileName2','Transonic','j24:j50023');
Output2b = xlsread('FileName2','Transonic','k24:k50023');
out2=Output2b-Output2a;
Force = Input;
U1=fft(Force);
Force2=Input2;
U2=fft(Force2);
Y1=fft(out1*10^3);
G1=Y1./U1;
Y2=fft(out2*10^3);
O2 = G1.*U2;
R1prime = ifft(O2);
figure(1)
plot(Time,R1prime,'b','linewidth',2)
hold on
plot(Time,out2*10^3,'r')
hold on
legend('FFT','Actual')
xlabel('time (sec)'); ylabel('Output (mV)')
```

.

B.4 Dynamic Responses at Different Sampling Rates for *NF*

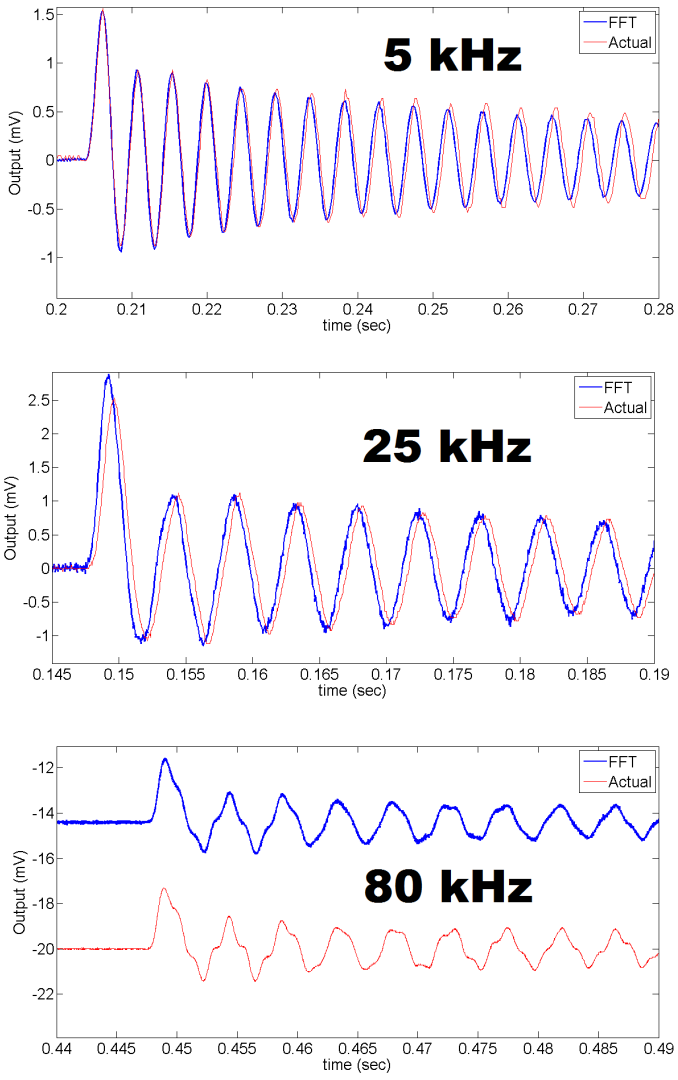

Figure B.2. Transformed data versus actual data for the *NF* component at 5 kHz, 25 kHz, and 80 kHz.

APPENDIX C

MATLAB PROGRAM FOR FORCE CALCULATIONS

MATLAB program for analyzing force measurements and test conditions

```
clc; clear all; format('long');
%% Input Offset Values
AOA=input('Angle of Attack [deg]:');
SSTstart=input('Start of Steady State [sec]:');
SSTend=input('End of Steady State [sec]:');
SampleRate = 50000; %frequency used for testing
Toff = 0; %offset for thermocouple
units = input('SI or ENG units [exact only]:','s');
    switch (units)
        case 'ENG'
            SI1 = 1; %lbf
            SI2 = 1; %inches
            SI3 = 1; %psi
            unit1 = 'lbf';
            unit2 = 'in.';
            unit3 = 'psi';
        case 'SI'
            SI1 = 4.44822; %lbf to Newtons
            SI2 = 0.0254; %inchs to meters
            SI3 = 6.894757; %psi to kPa
            unit1 = 'N';
            unit2 = 'm';
            unit3 = 'kPa';
        otherwise
            error('invalid option')
    end
A = 8.634956*(SI2^2); %0012 airfoil
RowStart=(SampleRate*SSTstart)+24; RowEnd=(SampleRate*SSTend)+24;
tic;
```

```
%% Reading the Document
%original data must be saved as an Excel file
TestData = ['FileNameLocation.xlsx']; SheetName = ['Transonic'];
time = xlsread(TestData,SheetName,'a24:a50023');
forcedata = xlsread(TestData,SheetName,'j24:n50023');
pressure1 = xlsread(TestData,SheetName,'b24:b50023');
pressure2 = xlsread(TestData,SheetName,'h24:h50023');
pressuretot = xlsread(TestData,SheetName,'f24:f50023');
static = xlsread(TestData,SheetName,'g24');
temp = xlsread(TestData,SheetName,'i24:i50023');

R1 = forcedata(:,1);
R2 = forcedata(:,2);
R3 = forcedata(:,3);
R4 = forcedata(:,4);
R5 = forcedata(:,5);

% offset is average of data points up to 0.05 sec
R1off = mean(R1(1:SampleRate*0.05))*10^3;
R2off = mean(R2(1:SampleRate*0.05))*10^3;
R3off = mean(R3(1:SampleRate*0.05))*10^3;
R4off = mean(R4(1:SampleRate*0.05))*10^3;
R5off = mean(R5(1:SampleRate*0.05))*10^3;

G1_NF=DynCalibFFT_NF(); %transfer function for NF
G1_CF=DynCalibFFT_CF(); %transfer function for CF

%% Finding Values of Components
S_nf = 642.46223;
S_mx = 131.94154;
```

```
S_cf = 11.385700;

S_mz = 119.27487;

S_pm = 26.039825;


NF = (((R2*10^3)-R2off)-((R1*10^3)-R1off))*S_nf;

MX = (((R2*10^3)-R2off)+((R1*10^3)-R1off))*S_mx;

CF = ((R3*10^3)-R3off)*S_cf;

MZ = ((R4*10^3)-R4off)*S_mz;

PM = ((R5*10^3)-R5off)*S_pm;


%% BALANCE MATRIX FROM STATIC CALIB.


%    NF            MX            CF            MZ            PM
M=[ 0.00000E+00   1.62914E+00 -1.32630E-03  -2.37747E-02 -1.24288E-02; %NF
   -4.82826E-05  -7.43067E-05 -1.34866E-06   2.18416E-05 -3.88019E-05; %NF^2
   -1.01484E-01   0.00000E+00 -2.09299E-05  -2.76365E-02  1.07950E-02; %MX
    2.93950E-05  -1.61264E-05  6.83769E-07  -2.68440E-05  3.27483E-05; %MX^2
   -4.03456E-05   4.39295E-05  8.73557E-08   5.44168E-05 -8.48497E-05; %NF*MX
   -9.81294E-02   1.17446E-02  3.74196E-03  -1.51792E-02  0.00000E+00; %PM
    2.03841E-04   6.36181E-05  2.00105E-06   1.69296E-05 -1.05052E-04; %PM^2
    4.19863E-05   4.46147E-04  2.80591E-05  -3.19131E-04  3.02033E-04; %NF*PM
   -2.37241E-01  -1.42972E-01  0.00000E+00   1.64027E+00  2.77195E-02; %CF
    6.86131E-04   9.53400E-04 -3.05192E-05   7.07454E-04 -1.83137E-03; %CF^2
    3.19279E-03  -4.45446E-03  2.23695E-02   0.00000E+00  1.76904E-03; %MZ
    1.86516E-03   1.78415E-03 -6.90900E-05  -2.87964E-04 -7.75144E-04; %MZ^2
   -4.92126E-03  -4.97230E-03  9.68641E-05   3.74891E-04  1.78986E-03]; %CF*MZ


n=length(R1);

tol=10^-3;

jmax=50;
```

```
%% Iteration Process

for i=1:n
    Ai=[NF(i); NF(i)^2; MX(i); MX(i)^2; NF(i)*MX(i); PM(i); PM(i)^2; NF(i)*PM(i);
     CF(i); CF(i)^2; MZ(i); MZ(i)^2; CF(i)*MZ(i)];
    Fun=[NF(i);MX(i);CF(i);MZ(i);PM(i)];
    Fnew=Fun-M'*Ai;

    for j =1:jmax
        Aj=[Fnew(1);Fnew(1)^2;Fnew(2);Fnew(2)^2;Fnew(1)*Fnew(2);Fnew(5);Fnew(5)^2;
         Fnew(1)*Fnew(5);Fnew(3);Fnew(3)^2;Fnew(4);Fnew(4)^2;Fnew(3)*Fnew(4)];
        Fnew_j=Fun-M'*Aj;
        if norm(Fnew_j-Fnew)<tol
            break
        end
        Fnew=Fnew_j;
    end
    jvect(i)=j;
   Forces(i,:)=Fnew;
   i=i+1;
end

%% filtering

%Low Bypass Filter
fc=100;% cut off frequency
fn=SampleRate/2; %nyquist frequency = sample frequency/2;
order = 5; %5th order filter, high pass
[b14 a14]=butter(order,(fc/fn),'low');
xf1=filtfilt(b14,a14,Forces(:,1));
xf2=filtfilt(b14,a14,Forces(:,2));
```

```
xf3=filtfilt(b14,a14,Forces(:,3));
xf4=filtfilt(b14,a14,Forces(:,4));
xf5=filtfilt(b14,a14,Forces(:,5));

%% USING THE TRANSFER FUNCTIONS (DYNAMIC CALIBRATION)

NF_x=Forces(:,1)./S_nf;
Y_nf=fft(NF_x);
U_nf=Y_nf./G1_NF;
NF_x1=ifft(U_nf);
NF_diff=mean(NF_x1(1:SampleRate*0.05)-NF_x(1:SampleRate*0.05));
NF_x1=NF_x1-(NF_diff);
nf1=filtfilt(b14,a14,NF_x1);
NF_new=NF_x1*S_nf;
NF_filt=nf1*S_nf;

CF_x=Forces(:,3)./S_cf;
Y_cf=fft(CF_x);
U_cf=Y_cf./G1_CF;
CF_x1=ifft(U_cf);
CF_diff=mean(CF_x1(1:SampleRate*0.05)-CF_x(1:SampleRate*0.05));
CF_x1=CF_x1-(CF_diff);
cf3=filtfilt(b14,a14,CF_x1);
CF_new=CF_x1*S_cf;
CF_filt=cf3*S_cf;

%% Pressure and Temperature data for Test Section
Ps= (static-0.5)*100+10.16;
P1 = pressure1.*204.58+0.6+Ps;
P2 = pressure2.*198.926+0.5+Ps;
Ptot = pressuretot.*203.335+1.0+Ps;
```

```
deltaP1 = Ptot./P1;
deltaP2 = Ptot./P2;
Mach1 = sqrt((2/0.4)*(deltaP1.^(0.4/1.4)-1));
Mach2 = sqrt((2/0.4)*(deltaP2.^(0.4/1.4)-1));

T1 = (temp-Toff+273.15)./(1+0.2*Mach1.^2);
mu1 = (1.462e-6*T1.^(3/2))./(T1+112);
V1 = Mach1.*sqrt(1.4*289*T1);
Re1 = (V1./mu1).*((P1./T1).*(6895/289))*0.0508;

T2 = (temp-Toff+273.15)./(1+0.2*Mach2.^2);
mu2 = (1.462e-6*T2.^(3/2))./(T2+112);
V2 = Mach2.*sqrt(1.4*289*T2);
Re2 = (V2./mu2).*((P2./T2).*(6895/289))*0.0508;

q2 = 0.5*1.4*P2.*Mach2.^2;

%% Time to Calculate Data
tElapsed = toc;
disp(['Seconds to run program:',num2str(tElapsed)]);
disp(['Number of iterations used for 10^-3 tolerance:', num2str(max(jvect))]);

%% PLOTS OF THE DATA

figure(1)
% plot(time,Forces(:,1))
hold on
plot(time,xf1*SI1,'b','linewidth',2)
plot(time,NF_filt*SI1,'r','linewidth',2)
xlabel('time (sec)')
```

```
ylabel({'NF' unit1})
legend('Raw','Filtered')
saveas(figure(1),'NF.png')
hold off

figure(2)
% plot(time,Forces(:,2))
hold on
plot(time,xf2*SI1*SI2,'b','linewidth',2)
xlabel('time (sec)')
ylabel({'MX' [unit1 unit2]})
saveas(figure(2),'MX.png')
hold off

figure(3)
% plot(time,Forces(:,3))
hold on
plot(time,xf3*SI1,'b','linewidth',2)
plot(time,CF_filt*SI1,'r','linewidth',2)
% title('Chord Force')
xlabel('time (sec)')
ylabel({'CF' unit1})
legend('Raw','Filtered')
saveas(figure(3),'CF.png')
hold off

figure(4)
% plot(time,Forces(:,4))
hold on
plot(time,xf4*SI1*SI2,'b','linewidth',2)
xlabel('time (sec)')
```

```
ylabel({'MZ' [unit1 unit2]})
saveas(figure(4),'MZ.png')
hold off

figure(5)
% plot(time,Forces(:,5))
hold on
plot(time,xf5*SI1*SI2,'r','linewidth',2)
xlabel('time (sec)')
ylabel({'PM' [unit1 unit2]})
saveas(figure(5),'PM.png')
hold off

figure(6)
plot(time,P1*SI3,'b')
hold on
plot(time,P2*SI3,'r')
legend('P1','P2')
xlabel('time (sec)')
ylabel({'Pressure' unit3})
axis([0.1 0.4 20 400])

figure(7)
plot(time,Mach1,'b')
hold on
plot(time,Mach2,'r')
legend('M1','M2')
xlabel('time (sec)')
ylabel('Mach Number')
axis([0.1 0.4 0 1])
```

```
figure(8)
plot(time,Re1,'b')
hold on
plot(time,Re2,'r')
legend('Re1','Re2')
xlabel('time (sec)')
ylabel('Reynolds Number')
axis([0.1 0.4 0 6e6])

% figure(9)
% plot(time,T1,time,T2)
% title('Temperature [K]')
% legend('T1','T2')
% xlabel('time (sec)')
% ylabel('Temperature [K]')
% axis([0.1 0.4 250 290])

%% Cl and Cd calculations

% Test Condition Averages
xM1 = mean(Mach1(RowStart:RowEnd))
xM2 = mean(Mach2(RowStart:RowEnd))
xRe1 = mean(Re1(RowStart:RowEnd))
xRe2 = mean(Re2(RowStart:RowEnd))
xq2 = (mean(q2(RowStart:RowEnd)))*SI3;
if SI3 > 1
    xq2 = xq2*10^3
else
    xq2
end
%test condition vectors
```

```
M1vect=Mach1(RowStart:RowEnd);
M2vect=Mach2(RowStart:RowEnd);
Re1vect=Re1(RowStart:RowEnd);
Re2vect=Re2(RowStart:RowEnd);
q2vect=q2(RowStart:RowEnd);
%filtered force vectors
NFvect=xf1(RowStart:RowEnd,1);
MXvect=xf2(RowStart:RowEnd,1);
CFvect=xf3(RowStart:RowEnd,1);
MZvect=xf4(RowStart:RowEnd,1);
PMvect=xf5(RowStart:RowEnd,1);
%dyn calib force vectors
NFvect1=NF_filt(RowStart:RowEnd,1);
CFvect1=CF_filt(RowStart:RowEnd,1);

%Force Averages
NFavg=(mean(NFvect))*SI1
NF_f_avg=(mean(NFvect1))*SI1
MXavg=(mean(MXvect))*SI1*SI2
CFavg=(mean(CFvect))*SI1
CF_f_avg=(mean(CFvect1))*SI1
MZavg=(mean(MZvect))*SI1*SI2
PMavg=(mean(PMvect))*SI1*SI2

% aerodynamic coefficients (corrected for orientation) (filtered raw)
cn=-NFavg/(xq2*A)
ca=-CFavg/(xq2*A)
cm=-PMavg/(xq2*A*2*SI2)
cl=cn*cos(AOA*pi/180)-ca*sin(AOA*pi/180)
cd=cn*sin(AOA*pi/180)+ca*cos(AOA*pi/180)
LDratio=cl/cd
```

```
% aerodynamic coefficients (dyn calib)
cn_f=-NF_f_avg/(xq2*A)
ca_f=-CF_f_avg/(xq2*A)
cm_f=cm
% cm_f=PM_f_avg/(xq2*A*2)
cl_f=cn_f*cos(AOA*pi/180)-ca_f*sin(AOA*pi/180)
cd_f=cn_f*sin(AOA*pi/180)+ca_f*cos(AOA*pi/180)
LDratio_f=cl_f/cd_f

%% Variation of coefficients with time
% cn1=xf1./(q2*A);
% ca1=xf3./(q2*A);
% cm1=xf5./(q2*A);
% cl1=cn1.*cos(AOA*pi/180)-ca1.*sin(AOA*pi/180);
% cd1=cn1.*sin(AOA*pi/180)+ca1.*cos(AOA*pi/180);
% LDratio1=cl1./cd1;
%
% figure(10)
% plot(time,cl1,time,cd1,time,cm1)
% title('Coefficient of Lift')
% xlabel('time (sec)')
% ylabel('cl')
% legend('cl','cd','cm')
% axis([0.10 0.30 -1.3 0.2])
%
% figure(11)
% plot(time,LDratio1)
% title('L/D ratio')
% xlabel('time (sec)')
% ylabel('L/D')
% axis([0.10 0.30 0 15])
```

```
%% Error Analysis
for i = 1:length(M1vect)
    error_M1(i) = (xM1-M1vect(i))^2;
    error_M2(i) = (xM2-M2vect(i))^2;
    error_Re1(i) = (xRe1-Re1vect(i))^2;
    error_Re2(i) = (xRe2-Re2vect(i))^2;
    error_q2(i) = (xq2-q2vect(i))^2;
end
    Merr1 = 2*sqrt(sum(error_M1)/length(M1vect));
    Merr2 = 2*sqrt(sum(error_M2)/length(M2vect));
    Re_err1 = 2*sqrt(sum(error_Re1)/length(Re1vect));
    Re_err2 = 2*sqrt(sum(error_Re2)/length(Re2vect));
    q_err2 = (2*sqrt(sum(error_q2)/length(q2vect)));

for i = 1:length(NFvect1)
    error_NF(i) = (NFavg-NFvect(i))^2;
    error_CF(i) = (CFavg-CFvect(i))^2;
    error_NF_f(i) = (NF_f_avg-NFvect1(i))^2;
    error_CF_f(i) = (CF_f_avg-CFvect1(i))^2;
    error_PM(i) = (PMavg-PMvect(i))^2;
end
    NF_err = (2*sqrt(sum(error_NF)/length(NFvect)));
    CF_err = (2*sqrt(sum(error_CF)/length(CFvect)));
    NF_err_f = (2*sqrt(sum(error_NF_f)/length(NFvect1)));
    CF_err_f = (2*sqrt(sum(error_CF_f)/length(CFvect1)));
    PM_err = (2*sqrt(sum(error_PM)/length(PMvect)));

    u_ca = sqrt((1/(xq2*A)*CF_err_f)^2+(-CF_f_avg/(xq2^2*A)*q_err2)^2)
    u_cn = sqrt((1/(xq2*A)*NF_err_f)^2+(-NF_f_avg/(xq2^2*A)*q_err2)^2)
    u_cl = sqrt((cos(AOA*pi/180)/(xq2*A)*NF_err_f)^2+
```

```
 (-sin(AOA*pi/180)/(xq2*A)*CF_err_f)^2
       +(-(NF_f_avg*cos(AOA*pi/180)-CF_f_avg*sin(AOA*pi/180))/
       (xq2^2*A)*q_err2)^2+((-NF_f_avg*sin(AOA*pi/180)-
       CF_f_avg*cos(AOA*pi/180))/(xq2*A)*(0.1*pi/180))^2)
u_cd = sqrt((sin(AOA*pi/180)/(xq2*A)*NF_err_f)^2+
       (cos(AOA*pi/180)/(xq2*A)*CF_err_f)^2+
       ((NF_f_avg*sin(AOA*pi/180)+CF_f_avg*cos(AOA*pi/180))/
       (xq2^2*A)*q_err2)^2+((NF_f_avg*cos(AOA*pi/180)-
       CF_f_avg*sin(AOA*pi/180))/(xq2*A)*(0.1*pi/180))^2)
u_cm = sqrt((1/(xq2*A*2)*PM_err)^2+(-PMavg/(xq2^2*A*2)*q_err2)^2)

disp('uncertainty and error calculations (u_c[]) work only when ENG units are used
to analyze the data.  Rerun the program with ENG units if uncertainty and
error values are needed.')
```

APPENDIX D

DATA FROM MINECK AND HARTWICH

D.1 Data from Mineck and Hartwich [6]

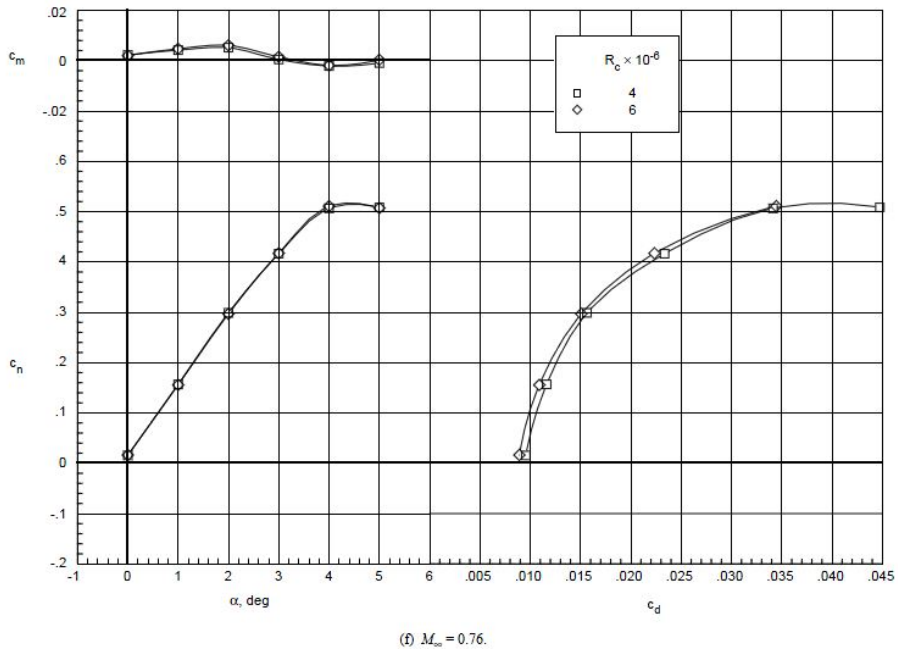

Figure D.1. Data for NACA 0012 airfoil at Mach 0.76 from Mineck and Hartwich.

REFERENCES

[1] Anonymous, "Aircraft Wallpaper," 2010. [Online]. Available: http://www.aircraft-wallpaper.com

[2] D. D. Baals and W. R. Corliss, *Wind Tunnels of NASA*. Washington, DC: NASA SP 440, 1981.

[3] J. J. Bertin and R. M. Cummings, *Aerodynamics for Engineers*. Upper Saddle River, NJ: Pearson, 2009.

[4] T. Balcazar, E. M. Braun, F. K. Lu, and D. R. Wilson, "Refurbishment and Testing Techniques in a Transonic Ludwieg Tunnel," no. AIAA-2011-1067, FL, Jan 2011.

[5] W. Stuessy, J. L. Peeples, and B. R. Mullins, "Improvements to the UTA high Reynolds number transonic wind," no. AIAA-1997-0663, Reno, NV, Jan 1997.

[6] R. E. Mineck and P. M. Hartwich, "Effect of Full-Chord Porosity on Aerodynamic Characteristics of the NACA 0012 Airfoil," NASA TR3591, Tech. Rep., 1996.

[7] H. Ludwieg, "Tube wind tunnel: A special type of blowdown tunnel," AGARD, Tech. Rep. AGARD-R-143, 1957.

[8] R. Jain, K. K. Ramakrishnan, and D. M. Chiu, "High Reynolds Number Research," Hampton, VA, Tech. Rep. NASA CP-2009, 1976.

[9] B. H. Goethert, *Transonic Wind Tunnel Testing*. Mineola, NY: Dover, 2007, Republication of 1961, on behalf of AGARD, NATO.

[10] J. Peeples, "Experimental investigation of the vortex structure of a prototype V-22 blade tip," Master's thesis, University of Texas at Arlington, 1997.

[11] C. Rath, "Wing Tip Vortex Stagnation Pressure Survey of Various Shapes," Master's thesis, University of Texas at Arlington, 1991.

[12] I. Kalkhoran, "An Experimental Investigation of the Perpendicular Vortex-Airfoil Interaction at Transonic Speeds," Ph.D. dissertation, University of Texas at Arlington, 1987.

[13] R. Starr and C. Schueler, "Experimental Studies of a Ludwieg Tube High Reynolds Number Transonic Tunnel," *AIAA Journal*, vol. 12 no.3, pp. 267–268, Mar 1974.

[14] S.-Y. Young, "Development of Calibration and Digital Filtering Procedures for a 5-Component Strain Gage Balance," Master's thesis, University of Texas at Arlington, 1991.

[15] W. Elbers, "Aerodynamic Investigation of Diamond Planforms," Master's thesis, University of Texas at Arlington, 1991.

[16] *1999 Transonic Manual for UTA Ludwieg Tube*, University of Texas at Arlington, 1999.

[17] J. C. Sivells, "Calculation of the Boundary Layer Growth in a Ludwieg Tube, Tech. Rep. AEDC-TR-75-118, 1975.

[18] "Technical Data for NI equipment," 2006, PCI-6023E, PXI-1036, PXI-6133, PXI-6722, SC-2345, SCC-Configuration Data.

[19] M. Robinson, J. M. Schramm, and K. Hannemann, "An investigation into internal and external force balance configurations for short duration wind tunnels," *Numerical and Experimental Fluid Mechanics*, vol. VI, pp. 129–136, NNFM 96 2007.

[20] N. Patel, "University of Texas Arlington 5-Component Balance Calibration Report," Modern Machine & Tool Company, Inc, Newport News, VA, Tech. Rep. 7396, May 1989.

[21] D. J. Mee, "Dynamic Calibration of Force Balances," Centre for Hypersonics, University of Queensland, Australia, Tech. Rep. 2002/6, Jan 2003.

[22] M. Robinson and K. Hannemann, "Short Duration Force Measurements in Impulse Facilities," in *25th AIAA Aerodynamic Measurement Technology Conference*, no. AIAA-2006-3439, San Francisco, CA, Jun 2006.

[23] M. Robinson, "Simultaneous Lift, Moment and Thrust Measurements on a Scramjet in Hypervelocity Flow," Ph.D. dissertation, University of Queensland, 2003.

[24] M. D. Greenberg, *Advanced Engineering Mathematics*. Upper Saddle River, NJ: Pearson, 1998.

[25] D. Mee, "Dynamic Calibration of Force Balances for Impulse Hypersonic Facilities," *Shock Waves*, vol. 12, pp. 443–455, Mar 2003.

[26] H. Kolsky, *Stress Waves in Solids*. Mineola, NY: Dover, 1963.

[27] R. S. Figliola and D. E. Beasley, *Theory and Design for Mechanical Measurements*. Hoboken, NJ: Wiley, 2006.

[28] Various, "Report of the High Reynolds Number Wind Tunnel Study Group of the Fluid Dynamics Panel, Tech. Rep. AGARD-R-35, 1971.

[29] J. D. Anderson, *Fundamentals of Aerodynamics*. New York,NY: McGraw-Hill, 2001.

[30] K. Juhany and A. Darji, "Force Measurement in a Ludwieg Tube Tunnel," *Journal of Spacecraft and Rockets*, vol. 44 no. 1, pp. 88–93, Jan 2007.

BIOGRAPHICAL STATEMENT

Michael Werling, Jr. received his Bachelor of Science in mechanical engineering from Louisiana Tech University in 2009. His organizational skills, attention to detail, sense of humor, and his fellow ARC co-workers assisted him in completing this graduate degree in a timely manner. He owes thanks to his success from the work of Ernst Mach, Osborne Reynolds, and Hayden Panettiere. In his spare time, he enjoys the outdoors, including golf, camping, and hiking.